Characteristics of Calcium-Aluminate Slags and Pig Iron Produced from Smelting-reduction of Low Grade Bauxites

Fabian Imanasa Azof[1], Leiv Kolbeinsen[2], Jafar Safarian[3]

1. PhD candidate

2. Professor

3. Associate Professor

Norwegian University of Science and Technology (NTNU), Department of Materials Science and Engineering, N-7491, Trondheim, Norway

Corresponding author: Fabian Imanasa Azof

Contact email: fabian.i.azof@ntnu.no

Abstract

Low grade bauxite ores are not favorable in the conventional Bayer process for alumina production, as they are producing more bauxite residue (red mud) and accompanying lower alumina yield than high grade ores. In the present work, the thermodynamics and characterization of calcium aluminate slags and pig iron produced from smelting-reduction of high iron and silica-containing bauxites are studied. Coke and limestone are used to reduce the iron oxide and adjust the basicity of slag during smelting. There is evidence that complete iron separation from bauxite is feasible through smelting-reduction process, and up to 99.9 pct of iron can be eliminated. Moreover, it is shown that silicon, titanium and other elements partial separation from the Al_2O_3-containing slag occurs. The phase compositions and the distribution of elements between the metal and slag phases provides information about the high temperature behavior of the bauxite components during smelting-reduction. Employing electron microscopy analysis, it is indicated that the morphology of $CaO \cdot Al_2O_3$, $12CaO \cdot 7Al_2O_3$, $2CaO \cdot Al_2O_3 \cdot SiO_2$, and $CaO \cdot Al_2O_3 \cdot SiO_2$ phases in the slag, as well as the complex oxides of Ca-Al-Si-Ti in slag behave differently as the mass ratio of $Al_2O_3/(Fe_2O_3 + SiO_2)$ in the bauxite changes. It is

also shown that the phases of slag produced from smelting-reduction below 5 $K \cdot s^{-1}$ of cooling rate are proper for further leaching process.

I. Background

Data from alumina processing industry shows a global average production of bauxite residue (red mud) as 1-1.5 ton per ton of alumina, or about 150 million ton of red mud is produced annually [1]. Lot of efforts have been made to valorize this most abundant industrial by-product in the world in building materials [2], using as the rare earth element's source [3], making green direct reduced iron (DRI) [4], consuming in inorganic polymers and pozzolanic material [5], and so on. However, none of those has moved to a large-scale commercial production due to economic reasons and particular challenges in processing the red mud. Thus, this caustic material is a prominent environmental issue and is a major concern on most of alumina refineries in the world, and obviously increasingly lower grade of bauxite (high iron and silica content) makes the situation even more challenging. In the Bayer process, the iron present in the ore is the main component involved in the production of red mud, while silica causes loss of caustic soda to the solvent due to the high reactivity of the compound. The compositions of the bauxite are important in determining the amount of lime that should be added in the mixtures and, eventually, the ratios of CaO/Al_2O_3 (C/A) in the slags.

In 1927, Harald Pedersen [6] patented a method to extract alumina from bauxite without yielding any red mud; an overall illustration of the process is shown in Fig. 1. This process was run commercially in Høyanger, Norway, during 1928-1969 with 17,000 ton of annual production before closing down [7]. During that period, other researchers had adapted the patent for utilizing ferruginous bauxite in Albany, [8] and a pilot-plant of alumina production from non-bauxitic source (clay) in Tennessee [9]. Years later, Miller and Irgens [10] also made preliminary studies on alumina refinery plant with 200,000 tons of annual production, based on the same process. The Pedersen process shows a promising potential for the prevention of red mud production, however, as per to date this process has been abandoned more than four decades. Lack of literature and scientific evidence, especially in smelting-reduction part, lead the present authors to investigate the process thoroughly.

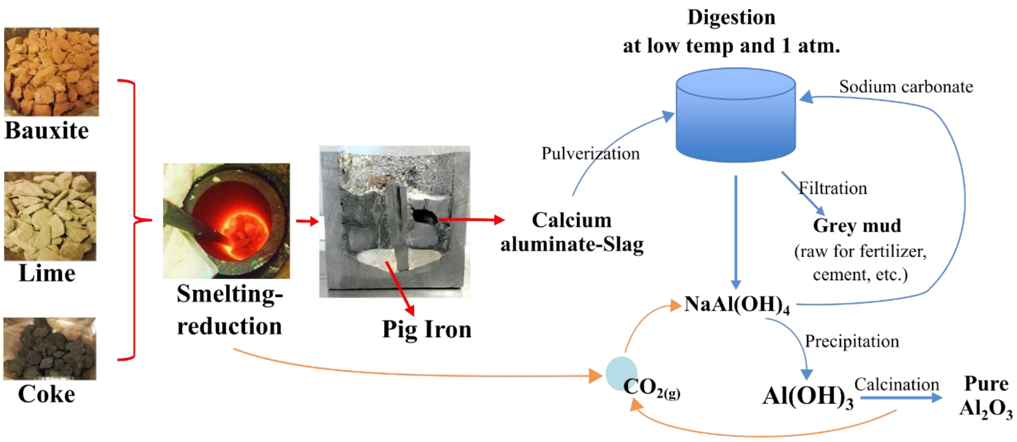

Fig. 1. An overview of Pedersen process.

II. Experimental Procedure

This section describes the applied experimental activities about the pyro-metallurgical part of the Pedersen process for treating selected low-grade bauxites. Consecutively, the procedure consists of materials preparation and characterization, and the details of smelting-reduction treatment.

II.1. Materials preparation and characterization

Mixture comprises bauxite ore, lime, and coke was prepared in laboratory scale. Three low grade of bauxite ores, named B-, G-, and I-Bauxite were used in different mixture. The characteristics of lime and coke based on the provider information is given in Table 1. The amounts of lime and coke used were based on the characteristics of the bauxites, and the lime/bauxite ratios for B-, G-, and I- are 0.55, 0.8, and 0.44, respectively.

Pig iron and slag are the products of the smelting-reduction treatment. For the targeted slag compositions, the CaO/Al_2O_3 (C/A) mass ratios were in the range of 0.65 to 0.75. This C/A ratio range is proper to obtain slag phases that has good leaching properties, as was reported in literatures [11] [12]. The amounts of coke in current work are 1.5 times larger than the stoichiometric needs to assure the complete reduction of iron oxides. Coke was dried in an oven at 373 K (100 °C) for 12 hours before use to remove any free-moisture content.

Part of the ores and products were ground by ring mill into powder size for phase identification using Bruker D8 A25 DaVinci™ X-ray Diffraction (XRD) with CuKα radiation, 10 - 75° diffraction angle, 0.01° step size, and 2.5° for both primary and secondary soller slit. The slag and pig iron samples were mounted in epoxy, polished, and carbon coated before employing Hitachi SU6600™ Scanning Electron Microscope (SEM) to capture the secondary electron (SE) and backscattered electron (BSE) images, X-ray element mapping, and use of Energy Dispersive Spectroscopy (EDS). X-ray Fluorescence (XRF) analysis was used to identify the overall composition of the ores and pig iron and slag products. Moreover, a JXA-8500F™ Electron Probe Micro-Analyzer (EPMA), supported by Wavelength Dispersive Spectroscopy (WDS), was applied for high accuracy on quantitative analysis of elements in selected phases of the products.

II.2. Smelting-reduction treatment

The mixture of starting materials was set into an open graphite crucible with 115 mm of inner diameter. The crucible was placed in a 75-kVA induction furnace and heated slowly at the rate of 5 $K.s^{-1}$ until it reached 1923 K (1650 °C). The partial pressure of gas (O_2, N_2, CO, CO_2, etc.) inside of the crucible was not measured during the smelting trial. However, an oxidizing atmosphere during smelting reduction process can be considered to exist because the experiments were in the open furnace~~However, an oxidizing atmosphere which contains partially CO_2 (g) and O_2 (g) may exist because of the oxidation of coke and crucible inside of the open furnace~~. The smelting-reduction duration was one hour at 1923 K (1650 °C), while the top of crucible was partially closed by refractories to minimize dissipation of the heat. However, the top was opened at intervals to crush the sintered materials or a solidified foamy-slag, while stirring of the melts was proper due to the induction in pig iron and gas bubbles movements in the slag. To compensate the heat loss, the mixture was heated until 2023 K (1750 °C) for the last ten minutes of the treatment. Consecutively, the mean and standard deviation of ~~mean smelting temperature of~~ B-, G-, and I-Bauxite smelting temperature is 1937 ± 44 K ~~(1664 °C)~~, 1935 ± 54 K ~~(1662 °C)~~, and 1910 ± 38 K ~~(1637 °C), respectively~~.

The crucible was then cooled to the room temperature inside the furnace while the power was off. To measure the temperature during the treatment a tungsten/rhenium thermocouple (type C), inside a graphite rod, and an encapsulating alumina insulation tube was used. About two- thirds of the materials smelted in the first one hour of treatment, and after it cooled down to room temperature the rest of materials were added and another one hour of treatment was started. For further analysis, the solidified materials and crucible were crushed to separate slag and metal from the crucible.

III. Results

Results comprises of four major parts; analysis of bauxites, smelting-reduction treatment, overall chemical compositions, and phase analysis in products.

III.1. Characteristics of bauxites

An XRD analysis of the bauxites are presented in Fig. 2. The mineralogy of B-Bauxite comprises of kaolinite, gibbsite, cristobalite, goethite, anatase, and magnetite. The first three shown as the dominant phases. G-Bauxite predominant phases are diaspore, boehmite, calcite, and hematite. It also has anatase as one of the gangue mineral. I-Bauxite is high in kaolinite and hematite, with relatively low in diaspore and boehmite compare to G-Bauxite. It is worth noting that I-Bauxite has the highest intensity of anatase peaks compared to the other two.

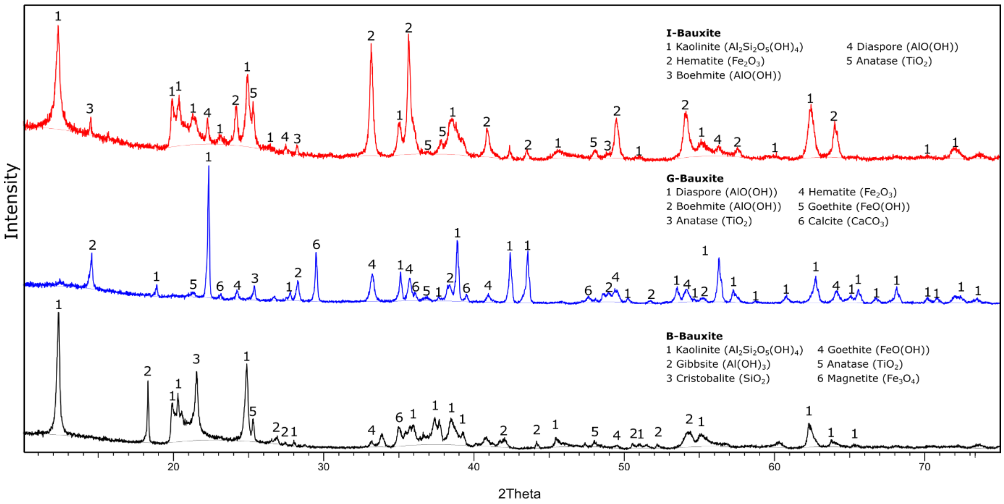

Fig. 2. XRD analysis of B-, G-, and I-Bauxites.

Table 2 shows the normalized XRF analysis result of B-, G-, and I-Bauxites. Three major elements that contribute to the bauxite leaching extent are aluminum, iron and silicon. These elements formed as either a hydroxide or oxide in bauxite as seen in XRD analysis presented above. The Loss of Ignition (LOI) content may decompose to air during smelting trial.

Prior to smelting, bauxite is obviously calcined at lower temperatures. Al_2O_3 and SiO_2 in calcined B- and I-Bauxite are formed as $Al_2O_3{\cdot}2SiO_2$, which is known as meta-kaolinite or aluminosilicate; a decomposed phase of kaolinite at high temperature. According to Kyriakogona et. al. [13] the degree of decomposition (dehydroxylation) is up to 98 pct when the calcination occurs at 1123 K (850 °C) in 60 min. Table 3 shows the normalized XRF analysis of the calcined bauxites, determined based on both XRF and XRD results.

III.2. Smelting-reduction behavior

The measurement of cooling rate was done from 1873 K (1600 °C) to 1573 K (1300 °C). As seen later in the $CaO\text{-}Al_2O_3\text{-}SiO_2$ ternary phase diagram, the latter temperature corresponds with the solidus line, which expectedly means no solidification occurs upon cooling to this temperature. The mean measured cooling rate is 4.9, 4.8, and 5 $K\cdot s^{-1}$ for B-, G-, and I-Bauxite, respectively. These cooling rates are well correlated with the masses (slag + iron) in the crucible where higher total mass shows slower cooling rate under similar conditions.

The cross section view of the solidified slag and pig iron in crucible after smelting-reduction trials are displayed in Fig. 3. The unreacted coke remaining on top of the slag is also illustrated. The separation of slag and iron produced from B-, G-, and I-Bauxite due to density differences is clearly seen. Obviously, coke particles are floating over the molten slag phase at elevated temperatures and thereafter. The different color appearance of the slags is mostly related to their different compositions. The volume pct of slag and pig iron produced from different bauxites also roughly measured by visual observation. As mentioned in experimental setup, the order of lime/bauxite mass ratio from the lowest to the highest is I-Slag, B-Slag, and G-Slag. It appears that the pct of slag increases and of pig iron decreases, considerably with increasing lime/bauxite mass ratio.

B-Bauxite

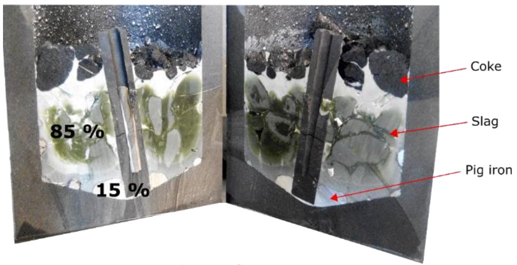

G-Bauxite

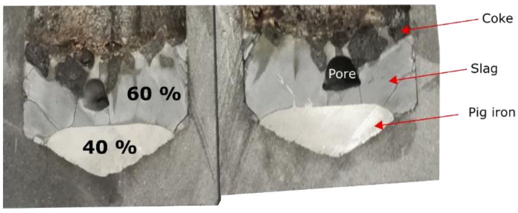

I-Bauxite

Fig. 3. Cross section view of the solidified slag and pig iron produced from B-, G-, and I-Bauxite.

In large-scale experiments, a useful performance indicator will be masses of slag and metal (pig iron) produced from a given mass and composition of raw materials. Mass change characteristics, including the correlation between losses of mass with the extent of smelting-reduction reaction are accordingly of great importance as a reference to large-scale experiments. Table 4 shows the changes of mass in different setups after smelting trial. Total mass loss pct for B-, G-, and I-Setup is 16.3, 15.4, and 6.1 pct, respectively. However, it becomes more interesting to see only the mass loss of starting materials during reaction and exclude the loss from both graphite crucible and rod. As can be seen, the estimated mass loss of materials after smelting trial is considerably high; 41.5, 39.4, and 21.2 pct for B-, G-, and I-Bauxite setup, respectively. Materials mass loss after the experiment might be caused by their LOI property, solid-gas transformation, i.e. $C \rightarrow CO_{(g)}$ or $CO_{2\,(g)}$, $CaCO_3 \rightarrow CaO$ +

$CO_{2\,(g)}$, and oxides phase reduction, i.e. $Fe_xO_y + yC \rightarrow xFe + yCO_{(g)}$, $SiO_y + yC \rightarrow Si + yCO_{(g)}$, $TiO_2 + 2C \rightarrow Ti + 2CO_{(g)}$.

III.3. Chemical compositions of products

The result of XRF analysis of the produced slags in Table 5 shows the mass balance and smelting of mixtures was done properly as the C/A ratio on each slag is in the expected range, as mentioned in experimental procedure. It is worth noting here the low FeO_x content in the slag, which agrees with our previous result [14]. Most of the reduced iron oxide becomes metal that saturated with carbon; pig iron. As seen in Table 6, the B-, G-, and I-Pig iron contains 89.9 - 92.7 wt pctFe and are saturated in carbon, and contain 0.2 - 4.0 wt pctSi, low trace of titanium and minor elements, i.e. V, Cr, P, S, are also observed. Most of the minor elements are derived from coke and lime. The saturated carbon content is estimated here based on the silicon content and the reliable solubility data for carbon in Fe-Si-C melts [15].

III.4. Phase and microstructural analysis of the products

Phase identification of the slags resulted from XRD analysis is shown in Fig. 4. B-Slag has $2CaO{\cdot}Al_2O_3{\cdot}SiO_2$ (C_2AS) and $CaO{\cdot}Al_2O_3$ (CA) as the primary and secondary phases, respectively. However, the latter phase seems to have another polymorph that bonds SiO_2 and MgO as be precisely identified later on BSE image. XRD analysis of G-Slag shows that the primary and secondary phase of the slag are $12CaO{\cdot}7Al_2O_3$ ($C_{12}A_7$), CA and $5CaO{\cdot}3Al_2O_3$ (C_5A_3), respectively. The latter phase is considered as an unstable phase that may be reformed to $C_{12}A_7$ phase at high temperature [16] [17]. In I-Slag, CAS phase appears as the dominant phase, followed by small fraction of silica phase.

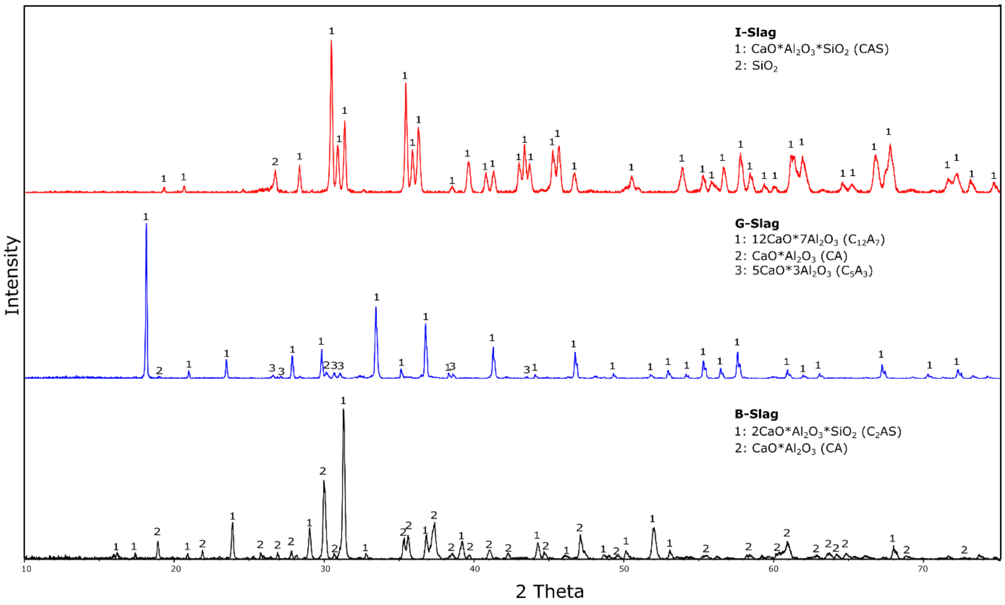

Fig. 4. XRD analysis on B-, G-, and I-Slag.

The X-ray element mapping element mapping of B-, G-, and I-Slag is shown in Fig. 5, Fig. 6, and Fig. 7, respectively. These figures show clearly the concentration extent of several elements in every structure that co-exists in slag. In B-Slag, calcium and silicon are more concentrated in the bright structure, which is later shown to be C_2AS phase. Aluminum is more concentrated in the dark area within the lamellar structure. Whereas, titanium and magnesium are dispersed uniformly. In G-Slag, the main structure ($C_{12}A_7$ phase) has more concentration of aluminum than other structures. Silicon and titanium are densely populated between large $C_{12}A_7$ grains. As can be seen there are structures that have complex oxides between Ca-Si-Ti elements. In contrast with B-Slag, magnesium is concentrated in spots. The X-ray element mapping of I-Slag shows that titanium, aluminum, and magnesium are highly concentrated in the dark structure. Obviously, bright structure has more concentration of calcium and silicon than the dark one. Two phases co-exist between the $C_{12}A_7$ particles in G-Slag. Therefore, it is necessary to examine the structures in higher magnification and analyze the composition by using SEM and EDS as the obtained results by these techniques are shown in Fig. 8. It shows that the area with bright and dark structure has more concentration of titanium than other structures in slag.

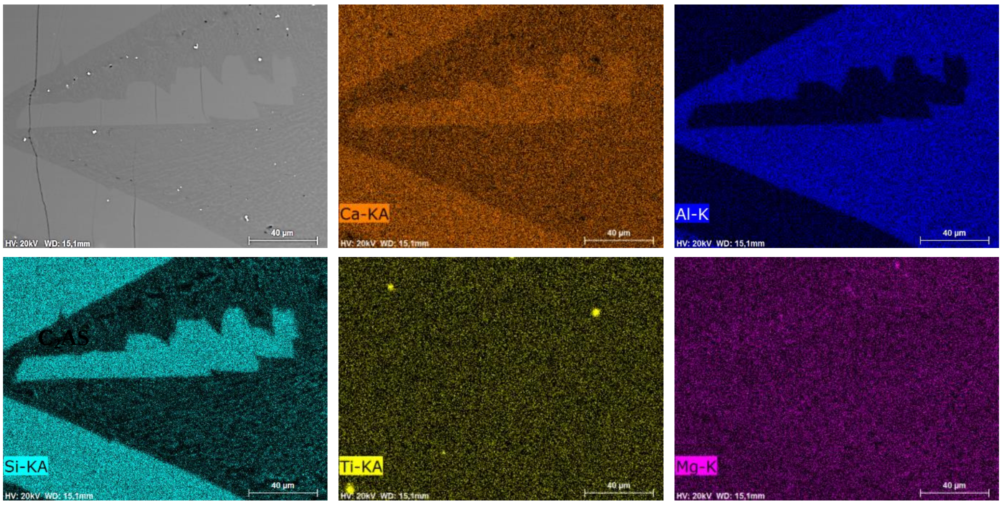

Fig. 5. X-ray element mapping of B-Slag.

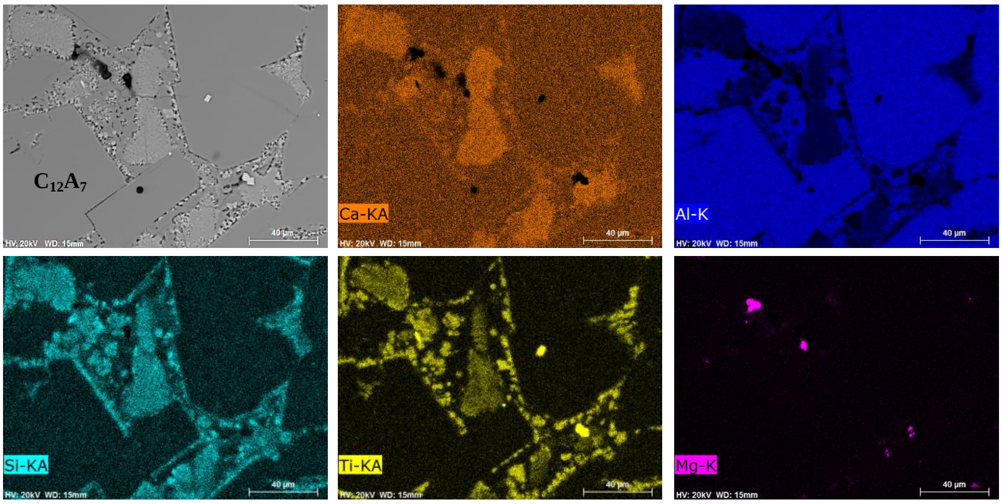

Fig. 6. X-ray element mapping of G-Slag.

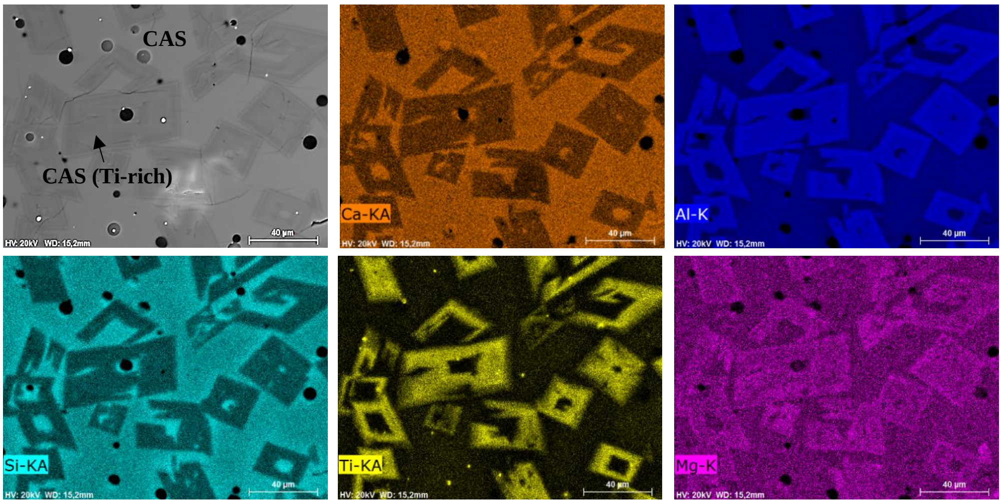

Fig. 7. X-ray element mapping of I-Slag.

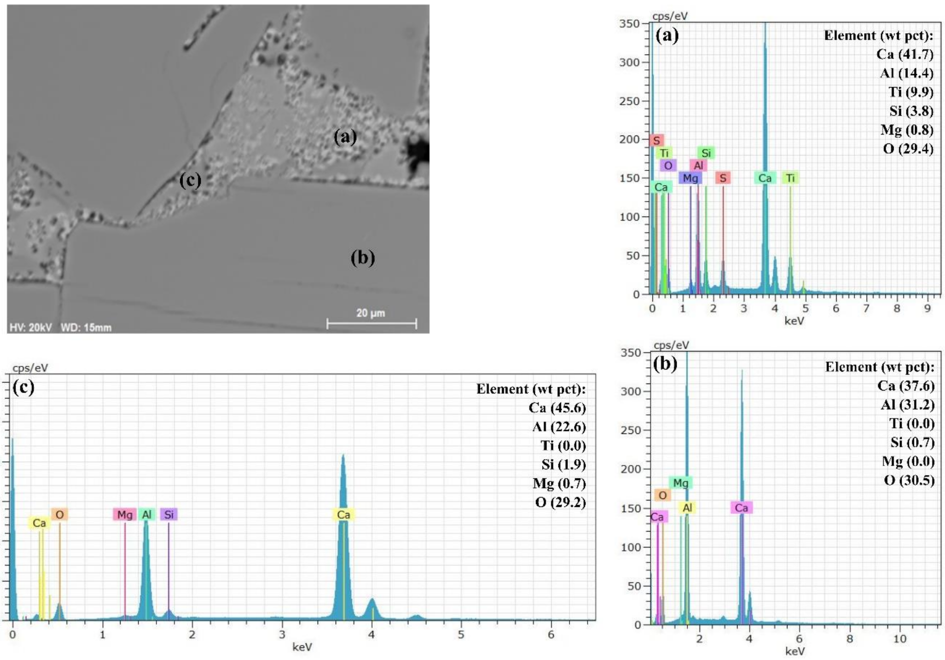

Fig. 8. BSE image of G-Slag with the corresponding EDS quantified analysis at (a), (b), and (c) area..

Fig. 9 (a), (b), and (c) show the BSE images of B-, G-, and I-Slag, respectively. As seen, three structures co-exist in the B-Slag and the two main structures are seen in each G- and I-Slag. Composition of each structure was measured by WDS analysis at 2 - 3 locations shown in Fig. 9. Table 7 presents the WDS analysis of the observed phases in Fig. 9. In average, concentration of CaO, Al_2O_3, SiO_2 constitute more than 95 wt pct of the slags. On the other hand, FeO content is low in all structures of slags, averaging around 300 ppm, which is in agreement with low measured FeO concentrations by XRF (Table ~~6~~5). Numbers (a)1 - 3, (a)4 - 6, and (a)7 - 9, are WDS results for the dark, fine lamellar and bright structure that are present in B-Slag (Fig. 9 (a)), respectively. Dark structure is composed by 43 wt pctCaO, 35 wt pctAl_2O_3, and 22 wt pctSiO_2 in average. Fine lamellar has similar composition as the dark structure has, which is 43 wt pctCaO, 35 wt pctAl_2O_3, and 21 wt pctSiO_2 in average. While bright structure is predominantly composed of 55 wt pctCaO and 31 wt pctTiO_2 in average. Number (b)1 - 3 and (b)4 - 6 are consecutively the composition of the bright-coarse grain and smaller grain which adjacent to a darker structure that showed in G-Slag (Fig. 9 (b)). The first structure has 50 wt pctCaO and 49 wt pctAl_2O_3 in average. The latter one has 49 wt pctCaO, 43 wt pctAl_2O_3, 3 wt pctSiO_2, and 4 wt pctTiO_2. Number (c)1 - 3 and (c)4 - 6 show the bright and dark structure in I-Slag (Fig. 9 (c)), respectively. In average, the bright structure is composed by 31 wt pctCaO, 32 wt pctAl_2O_3, 34 wt pctSiO_2, and 1 wt pctTiO_2. The dark structure shows that it has less CaO and more TiO_2 than the bright one has; 28 wt pctCaO, 34 wt pctAl_2O_3, 33 wt pctSiO_2, and 3 wt pctTiO_2. BSE in I-Slag indicates it has significant number of pores, which are not observed in the B- and G-Slags.

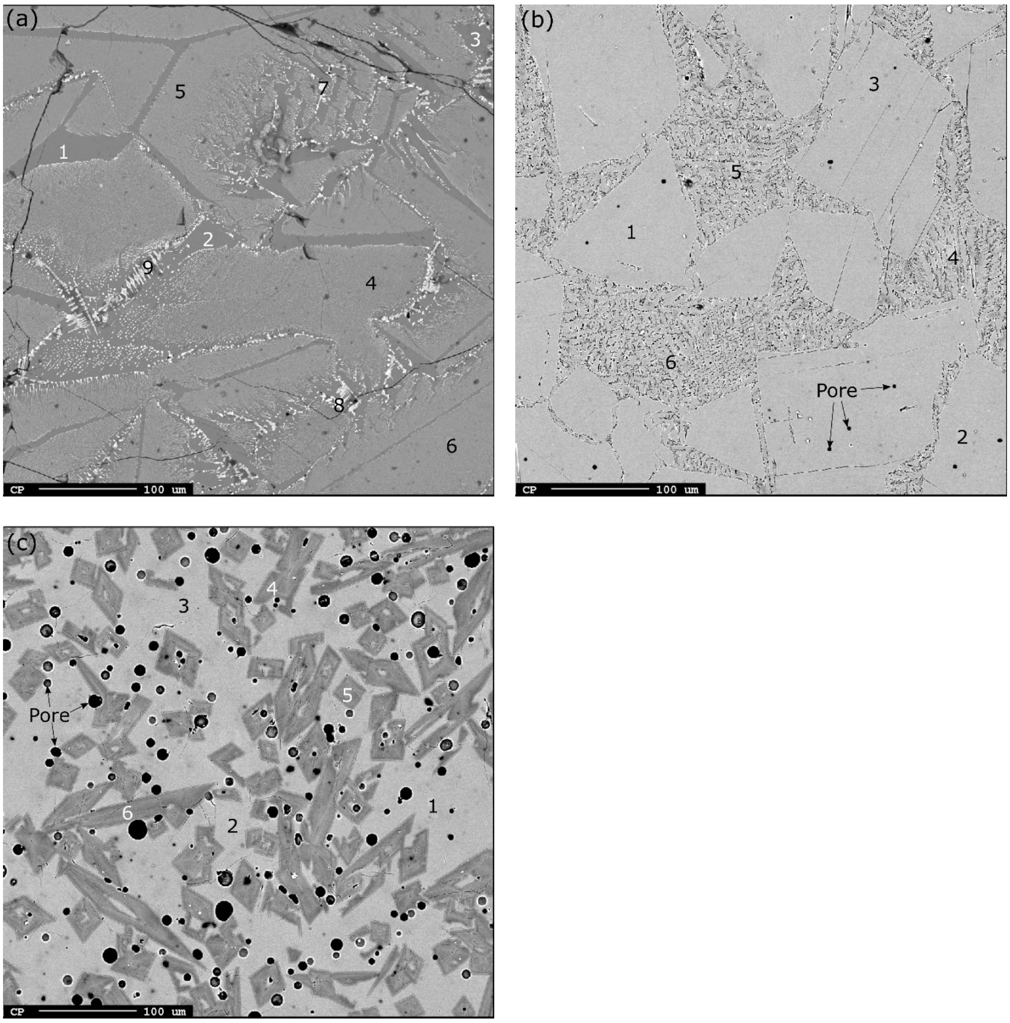

Fig. 9. BSE images of: (a) B-Slag, (b) G-Slag, and (c) I-Slag.

BSE image in Fig. 10 shows the cross-section of B-Slag and adjacent B-Pig iron. The light phase shows the Fe-metal of pig iron, while the grey and dark one show carbide and graphite phases, respectively. Table 8 shows the WDS analysis on the pointed phases. High concentration of titanium found in carbide phase. Vanadium, as one of the carbide former elements, concentrated in carbide phase~~ number 3 and 4~~, which is showed in point 3 and 4 in Fig. 10. Phosphorus and manganese are detected in Fe-metal matrix with 0.2 and 1.1 wt pct in average. Most of the manganese oxide is reduced to pig iron as it has low presence in slags, which is 800 ppm in average. Other trace elements showed in table are recognized as potassium and calcium. In addition, the lower magnification BSE image in Fig. 11 shows the metal matrix and co-existing phases in the produced metals.

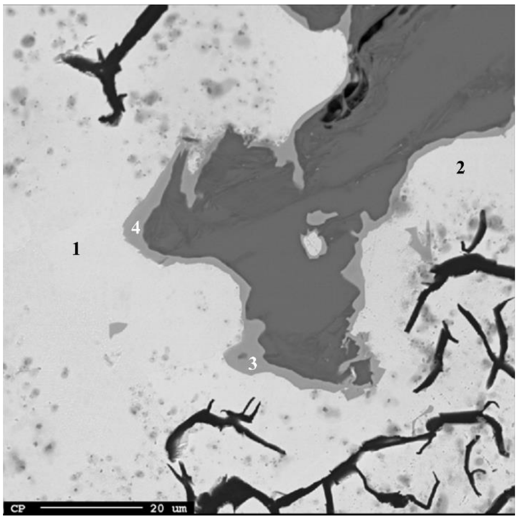

Fig. 10. BSE image of cross-section of B-Slag and adjacent B-Pig iron.

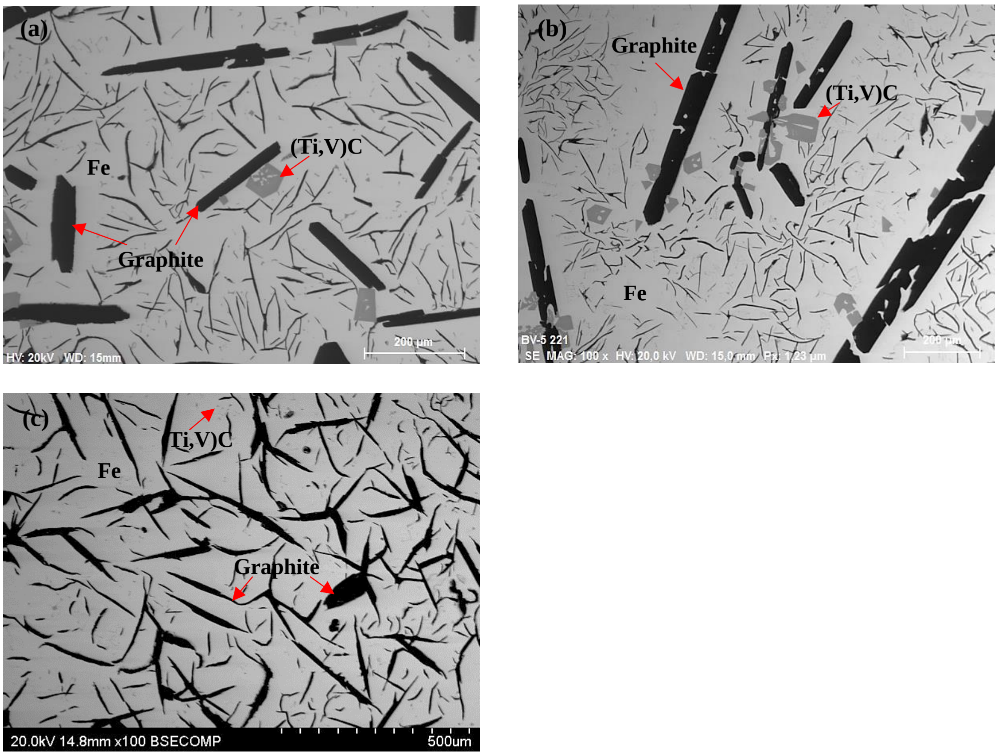

Fig. 11. BSE images showing the main co-existing phases in (a) B-; (b) G-; and (c) I-Pig iron samples.

IV. Discussion

In this section, mass changes before and after of experiment, thermochemistry of the reactions, distribution of elements in slag and pig iron, and slag characteristics are discussed.

IV.1. Mass balance

From the LOI data of each bauxite presented in Table 2, we can calculate the mass losses in B-, G-, and I-Bauxite due to the ignition, which is 0.28, 0.25, and 0.12 kg for the amounts used, respectively. The LOI data for lime due to the decomposition of lime into $CO_{2\ (g)}$ can be calculated based on the carbonate amount in the same table, which is 0.45, 0.66, and 0.23 kg for B-, G-, and I-Bauxite setup, respectively. While the moisture content of coke is removed after pre-heating in the oven before use, the LOI of coke is 1.53 wt pct as shown in Table 1, which gives loss as much as 2.10^{-3} kg.

Total loss due to transformation of C to CO $_{(g)}$ and oxides phase reduction can be calculated and given as 0.16, 0.21, and 0.16 kg for B-, G-, and I-Bauxite, respectively. This gives the theoretical mass loss for B-, G-, and I-Bauxite is, consecutively, 0.9, 1.13, and 0.52 kg. As seen in Table 9, the theoretical mass loss with the measured one shows proper correlation, in particular for G- and I-Bauxite. The difference between theoretical and measured mass loss in B-Bauxite might be due to the losses of SiO $_{(g)}$. Details of the explanation will be discussed in section IV.4.

IV.2. Smelting-reduction thermochemistry

Based on the XRD results in Fig. 2, B- and I-Bauxite are constructed mainly from kaolinite. This phase is found in either bauxite or non-bauxitic source; clay. Many works have been done to extract alumina from kaolinite with acid or alkaline solution [18] [19] [20]. In the Bayer process this is a major problem as the kaolinite is dissolved by sodium hydroxide solution which leads to high loss of caustic soda according to the following reaction:

$$Al_2Si_2O_5(OH)_{4\,(s)} + 6NaOH_{\,(l)} = 2Na_2SiO_{3\,(l)} + 2NaAl(OH)_{4\,(l)} + H_2O_{\,(l)} \qquad (1)$$

Furthermore, precipitation of the desilication products, i.e. sodalite ($Na_8(Al_6Si_6O_{24})Cl_2$), cancrinite ($Na_6Ca_2((CO_3)_2Al_6Si_6O_{24})\cdot 2H_2O$), etc. occur at elevated temperatures that are energy consuming. Low-grade of bauxites typically characterized with low Al_2O_3/SiO_2 mass ratio [18] [21] [22], and/or Al_2O_3/Fe_2O_3 mass ratio [23]. As both SiO_2 and Fe_2O_3 could be present in particular ore we may classify the low-grade bauxite based on its low $Al_2O_3/(Fe_2O_3 + SiO_2)$ mass ratio. According to the concentrations of calcined bauxites in Table 3, this ratio for B-, G-, and I-Bauxite is 0.8, 2.4, and 0.6, respectively. These bauxites also have certain amount of TiO_2 that later in the slag phase might affect the slag chemistry, its self-disintegration, and leachability [24]. The effect of MgO content of slag on leachability has also been reported as it becomes the main impurity in blast furnaces' slag [25]. However, in the present work the composition of Mg and remaining elements considered as trace elements that give least effect on the slag properties. According to the obtained XRF results presented in Table 5, 94.8 - 99.9 pct of Fe and Mn have been removed from the Al_2O_3-containing slag, together with parts of Si and Ti. Coke produces CO gas and dissolved carbon in molten iron, and carbon in both forms is the reductant for oxides in bauxite. In addition, the usage of graphite crucibles makes an additional carbon source for the carbothermic reduction. Based on the ores characteristics, the main smelting-reduction reactions that may take place are:

$$3Fe_2O_{3\,(s)} + C_{\,(s,\ dissolved)} = 2Fe_3O_{4\,(s)} + CO_{\,(g)} \tag{2}$$

$$3Fe_2O_{3\,(s)} + CO_{\,(g)} = 2Fe_3O_{4\,(s)} + CO_{2\,(g)} \tag{3}$$

$$Fe_3O_{4\,(s)} + C_{\,(s,\ dissolved)} = 3(FeO) + CO_{\,(g)} \tag{4}$$

$$Fe_3O_{4\,(s)} + CO_{\,(g)} = 3(FeO) + CO_{2\,(g)} \tag{5}$$

$$(FeO) + C_{\,(s,\ dissolved)} = Fe_{\,(l)} + CO_{\,(g)} \tag{6}$$

$$(SiO_2) + 2\underline{C} = \underline{Si} + 2CO_{\,(g)} \tag{7}$$

$$(SiO_2) + CO_{\,(g)} = SiO_{\,(g)} + CO_{2\,(g)} \tag{8}$$

$$(SiO_2) + \underline{Si} = 2SiO_{\,(g)} \tag{9}$$

$$SiO_{\,(g)} + \underline{C} = \underline{Si} + CO_{\,(g)} \tag{10}$$

$$\underline{(Ti}\cancel{\tfrac{1}{2}\,(Ti}O_2) + \underline{2}C_{\,(solid,\ dissolved)} = \cancel{\tfrac{1}{2}}\underline{Ti} + \underline{2}CO_{\,(g)} \tag{11}$$

Formatted: English (U.S.)

Formatted: Underline

Formatted: Underline

Formatted: Underline

$$(MnO) + \underline{C} = Mn + CO_{\,(g)} \tag{12}$$

$$C_{(s)} = \underline{C} \tag{13}$$

$$CO_{2\,(g)} + \underline{C} = 2CO_{(g)} \tag{14}$$

The underline "_" and parenthesis "()" notations denote the element or phase that is dissolved in the Fe-liquid solution and slag at known temperature, respectively. It is emphasized here that the reduction of Fe_2O_3 and Fe_3O_4 by $CO_{(g)}$ through reactions (3) and (5) is more feasible than reactions (2) and (4). FeO and even Fe can be also formed in solid state; however, we here assume that Fe is mainly produced from FeO in the slag. Reactions (6-10) show the reduction mechanism of FeO and SiO_2 at slag/gas, gas/metal, and slag/metal interfaces as observed by Pomfret and Grieveson [26], Teasdale and Hayes [27], and Safarian et al. [28]. A simple illustration can be given as in Fig. 12, where mass transport of the gaseous species (CO, CO_2, SiO) in gas bubbles at the slag/metal interface are very important.

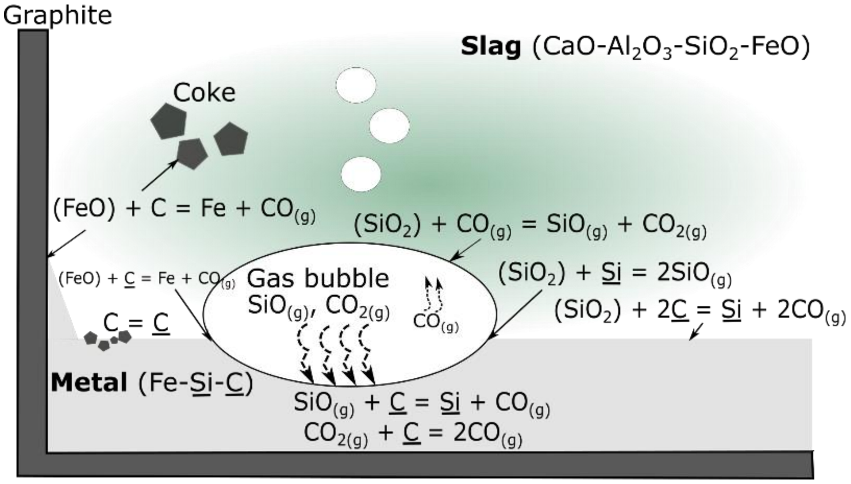

Fig. 12. Illustration of FeO and SiO_2 reduction by carbothermic reaction at slag/gas, gas/metal and slag/metal interface.

As lime flux was used for slag making, the main reactions that occur in the process through high temperature sintering and smelting can be expressed in reaction (15-22).

$$CaO_{(s)} + Al_2O_{3\,(s)} = (CaO\cdot Al_2O_3) \qquad (15)$$

$$CaO_{(s)} + \frac{1}{3}Al_2O_{3\,(s)} = \frac{1}{3}(3CaO\cdot Al_2O_3) \qquad (16)$$

$$CaO_{(s)} + \frac{7}{12}Al_2O_{3\,(s)} = \frac{1}{12}(12CaO\cdot 7Al_2O_3) \qquad (17)$$

$$\frac{1}{3}(3CaO\cdot Al_2O_3) + \frac{1}{4}Al_2O_{3\,(s)} = \frac{1}{12}(12CaO\cdot 7Al_2O_3) \qquad (18)$$

$$CaO_{(s)} + Al_2O_{3\,(s)} + SiO_{2\,(s)} = (CaO\cdot Al_2O_3\cdot SiO_2) \qquad (19)$$

$$CaO_{(s)} + Al_2O_{3\,(s)} + 2SiO_{2\,(s)} = (CaO\cdot Al_2O_3\cdot 2SiO_2) \qquad (20)$$

$$CaO_{(s)} + \frac{1}{2}Al_2O_{3\,(s)} + \frac{1}{2}SiO_{2\,(s)} = \frac{1}{2}(2CaO\cdot Al_2O_3\cdot SiO_2) \qquad (21)$$

$$CaO_{(s)} + TiO_{2\,(s)} = (CaTiO_3) \qquad (22)$$

Here we do not consider the FeO-containing phases in the slag, as we do not have much of it left in the final slag. For the sake of simplicity, the compounds that composing the slag are denoted as follows: CaO = C, Al_2O_3 = A, and SiO_2 = S. In thermodynamic perspective, the above reactions of pig iron and slag making formation and their competition are dependent on the Gibbs energy changes at particular temperature. The calculated Gibbs energy changes of the formation of the metal and slag components in pure state by using HSC^{TM} software. The reduction of pure iron oxides may occur below 1273 K (1000 ^{o}C). While silica and titania are phases that could be reduced by carbon at relatively high temperature, which means these two phases separation out of bauxite consume more energy than iron. Moreover, the reduction of silica by CO $_{(g)}$ is unlikely to occur, as the Gibbs energy changes is positive at any given temperature. The slag-making reactions (reaction (15-22)) are viable at low temperature and there is a large driving force for slag formation upon the heating of bauxite + lime to elevated temperatures. The WDS results in both slag and pig iron (Table 7 and Table 8) show the main phases are in solid solution form with certain solubility, instead of the pure ones. However, HSC^{TM} calculation is for pure substances and the real Gibbs energy changes for the slag making reactions may be even more negative than calculations.

The equilibrium phases in different mixtures that co-exist during and after the smelting–reduction can be calculated by thermodynamic software, FactSage^{TM}, at temperatures between 1273 - 2073 K (1000 - 1800 °C) with an increment of 283 K (10 °C) and 0.70 ± 0.05 of C/A ratios. As the calculation results in Fig. 13 indicate, the Fe-fcc phase co-exists with solidified slag of B, G, and I at 1273 K (1000 °C) to 1663 K (1390 °C). The lattice changes to Fe-bcc phase at about 1663 - 1803 K (1390 - 1530 °C) before it starts to melt. In the meantime, liquid slag phase appears at around 1473 K (1200 °C) and its amount increases significantly at 1673 - 1773 K (1400 - 1500 °C). B- and I-Slag should have similar solid slag phases that are stable at temperature below 1573 K (1300 °C) as seen in the Fig. 13. Consecutively, from highest to the lowest fraction of phase is CAS_2, C_2AS, $CaTiO_3$, $CaMg_2Al_{16}O_{27}$, $Ca_2Mg_2Al_{28}O_{46}$, and spinel. In addition, B-Slag has $CaAl_{12}O_{19}$ phase as well at 1673 K (1400 °C). The calculation of co-existing equilibrium phases in B- and I-Slag is not in agreement with the XRD results presented in section III. The reason of the disagreement might be related with the elements distribution during smelting-reduction trial that will be discussed in section IV.5.

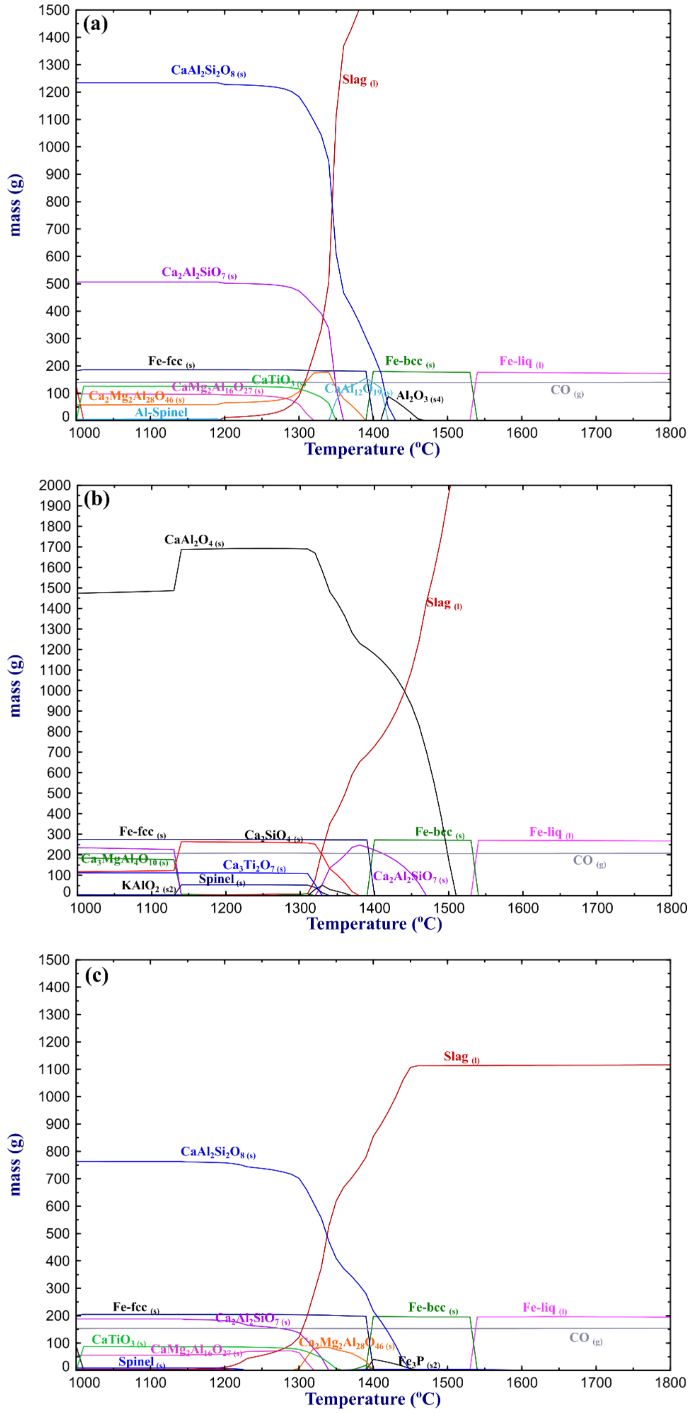

Fig. 13. The calculated phases in equilibria at different temperatures for: (a) B-Bauxite; (b) G-Bauxite; and (c) I-Bauxite setups.

G-Slag has CA phase constitutes about 70 wt pct of the slag phase, followed by low amount of C_2AS, $Ca_3MgAl_4O_{10}$, Ca_2SiO_4, $Ca_3Ti_2O_7$, spinel and $KAlO_2$. FactSage^{TM} does not recognize $C_{12}A_7$ phase in its database and it is the reason that this phase is absent in the equilibrium phases of G-Slag. Aside from $C_{12}A_7$ phase, the presence of CA phase is in agreement with the G-Slag XRD result. It is worth to note that the amount of TiO_2 and MgO of all obtained slags as in Table 5 is considerably low, which causes to not observe $CaTiO_3$, $CaMg_2Al_{16}O_{27}$, etc. in XRD analysis. However, the thermodynamic calculations here show that such phases may co-exist with the main recognized phases in the slags.

IV.3. Slag viscosity effect on porosity

The significant number of pores that appear in I-Slag in Fig. 9 (c) give strong indication of the gas formation during the oxides reduction by the mechanism illustrated in Fig. 12. The pores have been formed from the trapped gas that might come from the reduction reactions at the slag/metal interface. I-Slag has the highest amount of SiO_2 compared to others and the basicity based on CaO/SiO_2 (C/S) mass ratio is 0.9, which is relatively acidic. This slag forms networking oxides in melts that increases the viscosity and hinder the gas movement. In order to clarify this FactSage^{TM} was applied to calculate the viscosities of the obtained B-, G-, and I-Slags produced at 1923 K (1650 °C) and viscosities as 0.17, 0.10, and 0.48 Pa·s were obtained as shown in Fig. 14. The figure shows the correlation between different C/S mass ratios with the viscosity at 1723 K (1450 °C), 1823 K (1550 °C), and 1923 K (1650 °C) where C/A mass ratio equals to 1. It can be seen that by decreasing the temperature the viscosity is significantly increase especially at the C/S mass ratio less than 3. That is to say, the gas bubbles forming and leaving the slag/metal interface have more difficulties to rise in I-Slag than the others as the I-Slag has more gas hold-up capacity. It is worth mentioning that during the smelting-reduction experiments more foaming of the slag I was observed than the others, which is supporting the viscosity effect.

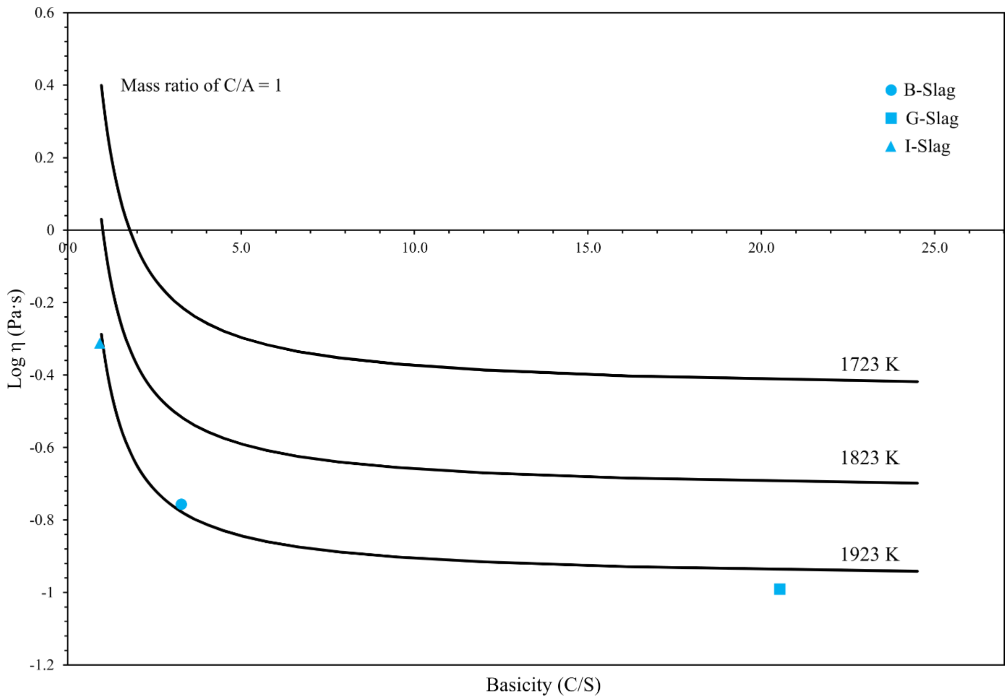

Fig. 14. Correlation between basicity (C/S) and viscosity in different C-A-S slags at different temperatures.

IV.4. Silica losses from slags

Formatted: English (U.S.)

The theoretical and measured mass loss difference in G- and I-Bauxite is relatively minor, while B-Bauxite shows otherwise (Table 9~~10~~). This indicates that another factor has contributed to the loss of mass in B-Bauxite that might be elaborated as follows:

According to the XRF analysis of bauxite, B- and I-Bauxite have identical concentration of SiO_2. It is worth to note that both have kaolinite as their main phase. Based on material balance calculation, total amount of silicon either in starting materials or the products produced from B- and I-Bauxite should be 0.29 and 0.17 kg, respectively. In fact, both of the bauxites show inequivalent amount of silicon in their input-output balance. The estimated losses of silicon in B- and I-Slag is 72.7 and 17.6 pct, respectively.

Silicon could be loss as a gas phase $SiO_{(g)}$, which is produced from reaction between SiO_2 in slag with carbon in the metal, as in reaction (23). Then it is leaving out from the slag when the gas bubble rises to the surface.

$$(SiO_2) + \underline{C} = SiO_{(g)} + CO_{(g)} \qquad (23)$$

The Gibbs energy change of formation in reaction (23) at 2023 K (1750 ^{o}C) is -2.2 kJ, which shows that high temperature is important factor in the silica gas production of the slag. As mentioned in the experimental procedure, the mean smelting temperature of B- is higher than of I-Bauxite. Silica loss could explain one of the reason why the concentration of silica in B- compare to I-Slag is lower, although the mixture setup before the smelting trial has identical C/(A+S) mass ratio that is 0.36 and 0.34 for B- and I-Bauxite, respectively.

IV.5. The distribution of elements between slag and pig iron

Based on equilibrium calculations in Fig. 13, the main phase of B- and I-slags at low temperature should be CAS_2 and C_2AS phase. In contrary, the XRD result in Fig. 4 shows the main phase for B- and I-Slag is C_2AS and CAS, respectively. The result is supported by XRF analysis of the products which shows different composition in slag and pig iron produced from B- and I-Bauxite, regardless the similar phase and C/A ratio of the bauxites mixture have before. This gives indication that during smelting-reduction and solidification of the melt the elemental distribution may act as a decisive factor on the final phases in slag.

Fig. 15 shows the distribution of phases in calcined bauxite ores and the corresponding slags after smelting-reduction according to the XRF results. The weight fraction of Al_2O_3 and SiO_2 phases remain the same before and after the treatment, which indicates the two phases are not easily reduced during the smelting-reduction treatment. The significant decreasing quantity of SiO_2 phase in B-Slag has already discussed in section IV.4. The CaO wt pct in G-Slag is higher than in other slags because of the high amount of lime used to maintain the required C/A ratio to get the leachable calcium aluminate phase.

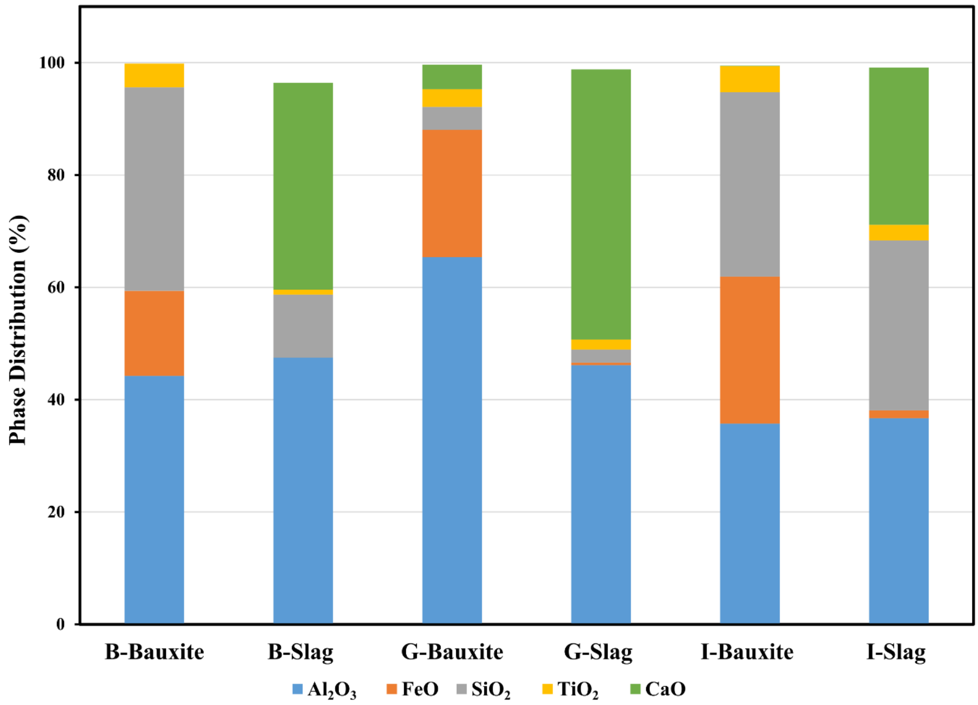

Fig. 15. Distribution of phases in bauxite ores and slags after smelting-reduction.

The reduction extent of each phase can be calculated by simple mathematical expression:

$$\text{Reduction extent (pct)} = \left[\frac{W}{W^\circ}\right] \times 100 \text{ pct} \qquad (24)$$

Where W° is mass of the amount of metal based on the stoichiometry, as if 100 pct reduced from an oxide and W is the actual amount of that metal present in the metal phase based on the XRF result of the pig iron. To make the mass loss based on the stoichiometry simple, we consider the iron reduction is 100 pct as the average WDS results of FeO content in all slags are low (see Table 7). Therefore, the SiO_2 reduction extent in B-, G-, and I-slag is 2.8, 1.3, and 1.6 pct, respectively. Higher SiO_2 reduction in B-Bauxite might be resulted from higher smelting temperature of this trial compare to G- and I-Bauxite as discussed above. According to HSC data, reaction (8) goes to the right side at temperature more than 1938 K (1665 °C), and based on the smelting temperature setup ~~in Fig. 2 the~~in section II.2., B-Bauxite was exposed in this temperature relatively longer than others were. From kinetics point of view, carbothermic reduction of SiO_2 from slag is much slower than that FeO. The other partially reduced phase was TiO_2. The TiO_2 reduction extent is 2.8, 8.4, 1.5 pct for B-, G-, and I-Bauxite, respectively. This calculation is in agreement with the amount of TiC that is observed in BSE image of the pig iron in Fig. 1~~2~~1. The reduction of TiO_2 in reaction (11) proceeds at around 2023 K (1750 °C) when pure substances are involved. However, as the activity of titanium in the molten iron is low, the reduction of TiO_2 may occur at the lower process temperature to some extent, yielding dissolved titanium in iron. Under carbon-saturated condition, the dissolved titanium has high possibility to make bond with the existing carbon and forms TiC during solidification of pig iron (reaction (25)). This is enhanced due to the low solubility of titanium in Fe-$C_{saturated}$-Ti system ~~The reduction of TiO_2 in reaction (11) proceeds at around 2023 K (1750 °C) when pure substances are involved. However, as the amount and activity of Ti in the molten iron is low, the reduction of TiO_2 may occur at the lower process temperature to some extent. Under carbon-saturated condition, the dissolved titanium has high possibility to make bond with the existing carbon and forms TiC during solidification of pig iron (reaction (25)). This is enhanced due to the low solubility of titanium in Fe-$C_{saturated}$-Ti system [29]~~[29].

Formatted: Subscript

Formatted: Subscript

Formatted: Subscript

$$\mathrm{Ti} + \mathrm{C} = \mathrm{TiC} \qquad \Delta G^{\circ}_{\cancel{25^{\circ}C}\,298\,K} = -180.8 \text{ kJ/mole Ti} \qquad (25)$$

Another mechanism for the formation of TiC particles can be the direct reaction of the dissolved carbon in the melt with TiO2 in the slag at slag/metal interface, as in reaction (26).

$$3\mathrm{C} + (\mathrm{TiO_2}) = \mathrm{TiC} + 2\mathrm{CO}_{(g)} \qquad \Delta G^{\circ}_{1873\,K} = -104.0 \text{ kJ/mole Ti} \qquad (26)$$

Formatted: English (U.S.)

Formatted: English (U.S.)

The thermodynamic activities given in reaction (11) and (26) are in standard condition with the titanium activity is unity. Therefore, we need to evaluate the reactions in a non-standard conditions, where we have a low titanium activity in the melt. For reactions (11) and (26) the expression of Gibbs energy changes can be written as:

$$\Delta G_{11} = \Delta G_{11}^{o} + RT \ln \frac{a_{Ti} \cdot pCO^{2}}{a_{TiO_2} . aC^{2}} \qquad (27)$$

$$\Delta G_{26} = \Delta G_{26}^{o} + RT \ln \frac{a_{TiC} \cdot pCO^{2}}{a_{TiO_2} . aC^{3}} \qquad (28)$$

Where $\Delta G_{11}°$ and $\Delta G_{26}°$ are the standard Gibbs energy changes of reactions (11) and (26), respectively. The activity of C and TiO_2 in the melt is unity and unknown, respectively. The partial pressure of $CO_{(g)}$ for both reactions is the same, thus equation (27) and (28) can be rearranged to

$$\Delta G_{11}^{o} + RT \ln a_{Ti} = \Delta G_{11} - RT \ln \frac{pCO^{2}}{a_{TiO_2} . aC^{2}} = \delta G_{11} \qquad (29)$$

$$\Delta G_{26}^{o} + RT \ln a_{TiC} = \Delta G_{26} - RT \ln \frac{pCO^{2}}{a_{TiO_2} . aC^{3}} = \delta G_{26} \qquad (30)$$

Since activity of TiC is unity, then equation (30) becomes

$$\Delta G_{26}^{o} = \Delta G_{26} - RT \ln \frac{pCO^{2}}{a_{TiO_2} . aC^{3}} = \delta G_{26} \qquad (31)$$

By comparing δG_{11} and δG_{26} values, we may predict which reaction is more favorable to occur in a particular temperature. We determine the activity of titanium in Fe-$C_{saturated}$-Ti system at 1873 K (1600 °C) from FactSage™ database and calculate the δG_{11} and δG_{26} in the melt, as seen in Fig. 16.

Formatted: Font: Not Italic
Formatted: Line spacing: Double
Formatted: Font: Not Italic
Formatted: Font: Not Italic
Formatted: Font: Not Italic
Formatted: Font: Not Italic
Formatted: Font: Not Italic
Formatted: Font: Not Italic
Formatted: Font: Not Italic
Formatted: Font: Not Italic
Formatted: Font: Not Italic
Formatted: Font: Not Italic
Formatted: Font: Not Italic
Formatted: Font: Not Italic
Formatted: Font: Not Italic
Formatted: Font: Not Italic
Formatted: Font: Not Italic
Formatted: Font: Not Italic
Formatted: Font: Not Italic
Formatted: Font: Not Italic
Formatted: Font: Not Italic
Formatted: Font: Not Italic
Formatted: Font: Not Italic
Formatted: Font: Not Italic
Formatted: Font: Not Italic
Formatted: Font: Not Italic
Formatted: Font: Not Italic
Formatted: Font: Not Italic
Formatted: Font: Not Italic
Formatted: Font: Not Italic
Formatted: Font: Not Italic
Formatted: Font: Not Italic
Formatted: Font: Not Italic
Formatted: Font: Not Italic
Formatted: Font: Not Italic
Formatted: Font: Not Italic
Formatted: Font: Not Italic
Formatted: Font: Not Italic

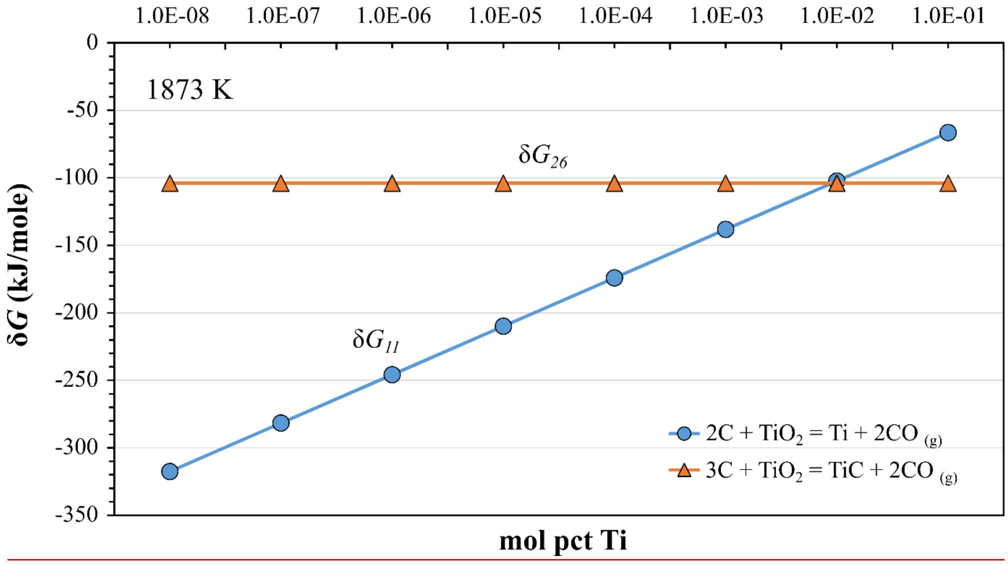

Fig. 16. The changes of δG_{11} and δG_{26} at 1873 K in different mol pct Ti.

Fig. 16 shows that if the amount of titanium in the melt is less than about 0.01 mol pct, the reaction (11) is more favorable than reaction (26), which means the TiO_2 is reduced and yields the dissolved titanium in the metal. In the contrary, if the titanium content is larger than about 0.01 mol pct then reaction (26) is more favorable than that of reaction (11), which means TiC formation at slag/metal interface is likely to occur.

As seen in WDS analysis of pig iron in Table 8, silicon content on number 1 and 2 of B-Pig iron show higher amount compare to that ~~in~~ of silicon content in I-Pig iron (Table 6). This confirms the result in XRF analysis and demonstrate the reduction mechanism of silica in bauxite during smelting-reduction. The WDS results ~~for Phase (2)~~of point number 3 and 4 show in Table 8 ~~in both images~~ confirmed the formation of (Ti,V)C in metal as was reported from literature ~~[7]~~[7]. As the solidus temperature of metal is lower than slag, the solute titanium in pig iron may segregate~~s~~ to the boundaries of metal and slag and forms carbide.

Formatted: Font color: Text 1

Formatted: Font color: Text 1

Formatted: Line spacing: Double

Formatted: Font: Not Italic, Font color: Text 1

Formatted: Font: Not Italic, Font color: Text 1

Formatted: Font color: Text 1

Formatted: Font: Not Italic, Font color: Text 1

Formatted: Font color: Text 1

Formatted: Centered

Formatted: Font: Not Italic

Formatted: Line spacing: Double

Another important parameter in studying the slag-metal systems is the distribution of the dissolved elements between the slag and metal phases and a distribution coefficient as L_i is defined, which is expressed as:

$$L_i = \frac{(\text{wt pct } i)}{[\text{wt pct } i]}$$

(~~2~~32~~5~~)

Where (wt pct *i*) and [wt pct *i*] are representing the mass pct of element *i* in the slag and metal phases, respectively. The distribution coefficient of Fe, Si, Ti, Mn, P, and V in current work is shown in Fig. 17~~6~~. Fe, Mn, P, and V have relatively low L_{Fe}, L_{Mn}, L_{P}, and L_{V} values (0 - 1.7), which gives indication that these elements stable in pig iron and shows that iron was 99.9 pct reduced. While the L_{Si} and L_{Ti} values vary depending on the type of bauxite and so the slag composition, which is 1.3 - 11.6 and 0.8 - 8.2 for L_{Si} and L_{Ti}, respectively. More experiments are necessary to have better understanding on the elements distribution in slag and pig iron produced from smelted bauxite.

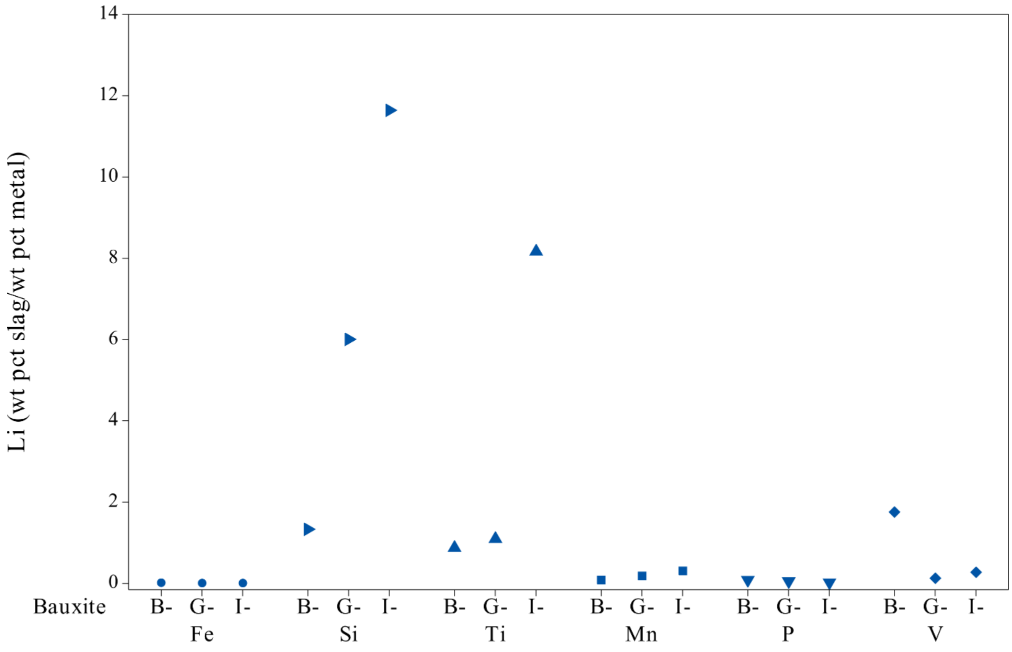

Fig. ~~16~~17. Distribution coefficient of several elements in different bauxites.

IV.6. Stable phases in the slag system

Even though the mixtures was set-up with particular ratio of C/A, the other compound, i.e. SiO_2 and TiO_2 affect the construction of phases in the slag system. As seen in Table 5, the main slag compounds are CaO, Al_2O_3, and SiO_2. While TiO_2 content is negligible (< 3 wt pct) and is not constructing of any new phase in the system [24]. Therefore, the slag is regarded here as a ternary $CaO\text{-}Al_2O_3\text{-}SiO_2$ system. Employing FactSage™ phase diagram module, the projection of isothermal sections from 1573 - 1873 K (1300 - 1600 °C) in $CaO\text{-}Al_2O_3\text{-}SiO_2$ system can be made as seen in Fig. ~~17~~18. Due to the limitation of compound database in FactSage, $C_{12}A_7$ phase is not shown in the projection. However, we draw the area of $C_{12}A_7$ phase manually into the ternary system (colored in pink) based on provided information in literature [17] [30].

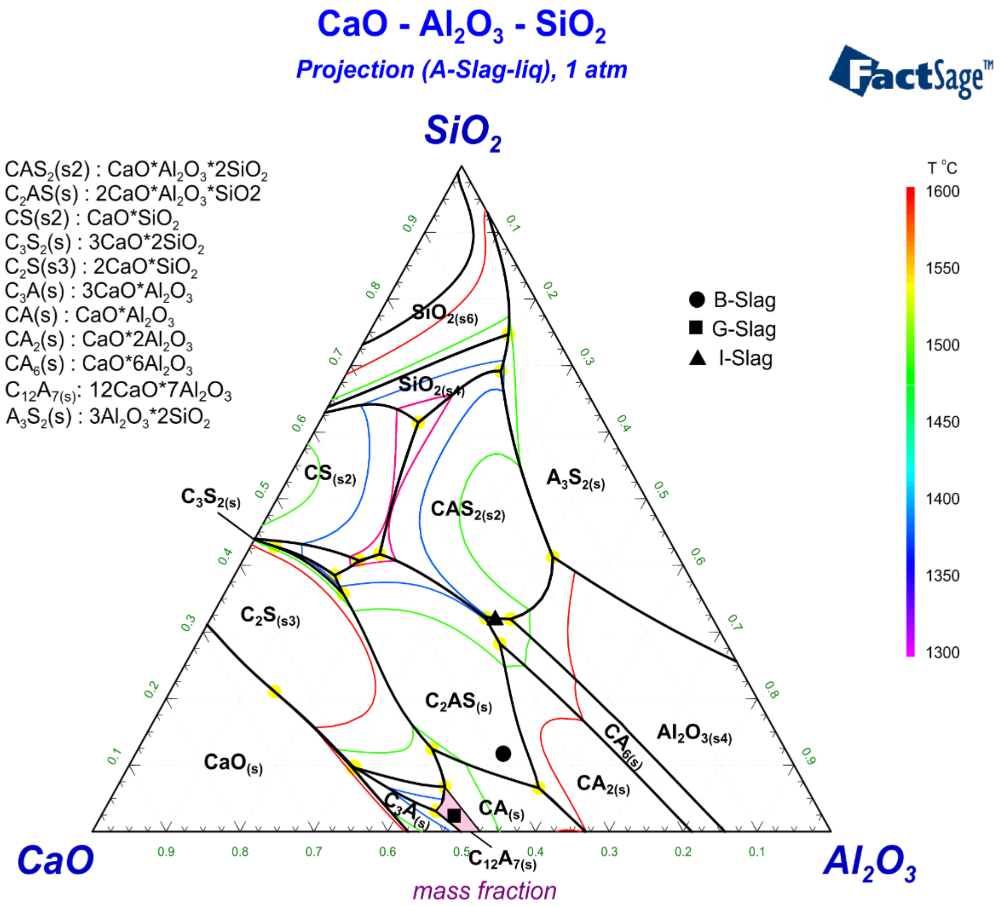

Fig. ~~17~~18. Isothermal projection of ternary CaO-Al$_2$O$_3$-SiO$_2$ system.

The calculated ternary phase diagram corresponds with the XRD result of B-Slag in Fig. 4. The direction of crystallization path goes toward the peritectic temperature and shows that C$_2$AS, CA, and β-C$_2$S phase are in equilibrium as condensed phases after solidification. However, neither β-C$_2$S nor γ-C$_2$S phases are traced in it. No existence of C$_2$S may be the reason why self-disintegration did not happen during cooling, as we observed. The self-disintegration of slag occurs due to the volume expansion by 12 pct as the crystalline phase transforms from β-C$_2$S to γ-C$_2$S [24] [31]. In a calcium aluminate containing-slag produced from blast furnace, it is reported that when the cooling rate is lower than 4.8 K.s^{-1} then the major phases of the slag are C$_{12}$A$_7$, γ-C$_2$S, and CA [32]. On the other hand, if the cooling rate is considerably high, 4.8 - 5.4 K·s^{-1}, the formation of C$_2$AS occurs. In present work, the cooling rate averages were above $4.8\ \mathrm{K{\cdot}s^{-1}}$. Another possible explanation would be related to low presence of β-C_2S in B-Slag (< 5 pct), as calculated in section IV.7, which is confirmed by no observation of the corresponding peaks in XRD spectrums (Fig. 4).

Based on the XRD result, G-Slag has $C_{12}A_7$, CA, and low fraction of C_5A_3 phase. The $C_{12}A_7$ phase was first observed by Rankin and Wright [33] in 1915 and has been in several discussions ever since. In 1965, Nurse et al. [34] observed that $C_{12}A_7$ phase is unstable in anhydrous or moist-free CaO-Al_2O_3 system, as it is in equilibria with H_2O above 1223 K (950 °C) and forms $Ca_{12}Al_{14}O_{32}(OH)_2$ when is fully saturated; the water present as hydroxyl ions in crystal structure. Later on, Haccuria et al. [35] showed that in a dry and high-purity (99.999 pct) argon atmosphere the formation of $C_{12}A_7$ phase does not occur. Here in G-Slag, $C_{12}A_7$ phase is observed in its anhydrous form where the data given as follows: a = 11.99856 Å, V = 1727.38 $Å^3$, density = 3.10^{-3} $\mathrm{kg.m^{-3}}$, in cubic I-43d (220) space group. The phase in the slag samples have been formed in an open furnace and oxidizing atmosphere, which subsequently is cooled to room temperature. The result is in agreement with Imlach et al. [36], who said the $C_{12}A_7$ phase might be stable at high temperatures as it absorbs excess of oxygen from any oxidizing atmosphere, even where pO_2 is as low as 10^{-3} Pa (10^{-8} bar). This finding is important to the study of calcium-aluminate slag making, as $C_{12}A_7$ phase is known as one of the leachable phase in CaO-Al_2O_3 system [8] [11] ~~[8]~~ [17] [37] and is, therefore, crucial to Pedersen process. Hallstedt [16] optimized the thermodynamic data of $C_{12}A_7$ phase and said that it melts congruently at 1449 °C. It has a eutectic with other phases C_3A and CA on each side, as seen in Fig. ~~18~~ 19 (a). In our results, G-Slag consists mainly of 46.1 wt pct Al_2O_3 and 48.1 wt pct CaO, which means according to Fig. ~~18~~ 19 (a) it may rather have C_3A and $C_{12}A_7$ than $C_{12}A_7$ and CA phase. However, Hallstedt considers only the binary system of CaO-Al_2O_3 and not the role of other constituents as if any involved; silica, titania, etc . Moreover, C_3A phase is relatively unstable as it can be reacted with free-Al_2O_3 in the system to form $C_{12}A_7$ (see reaction (18)). In our previous work [12] we did not observe the presence of $C_{12}A_7$ phase in a slag that was synthesized at high temperature and oxidizing atmosphere. The composition was 38 wt pct and 62 wt pct of CaO and Al_2O_3, respectively. Instead of the occurrence of CA and

$C_{12}A_7$ phase, the encountered phases were CA and C_3A that agrees with a moisture-free binary diagram as in Fig. 19~~8~~ (b).

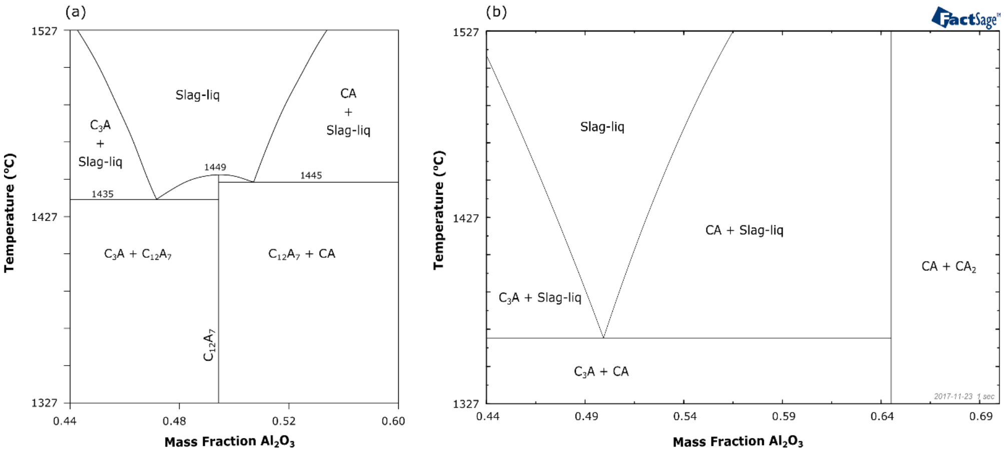

Fig. ~~18~~19. Part of CaO-Al_2O_3 binary system where (a) the $C_{12}A_7$ phase is included, and (b) a moisture-free without formation of $C_{12}A_7$ phase, as simulated by FactSage™.

The reason of this different phenomenon can be explained as follows:

1. In our previous work [12], CA phase was the primary crystallized phase (91 wt pct by phase lever-rule), and when the cooling reached eutectic temperature the remaining liquid may precipitate the $C_{12}A_7$ phase at grain boundaries. However, the amount of this phase was low (< 10 wt pct) and either it was dissolved in the adjacent CA phase or is dissociated to CA and C_3A phase at lower temperature as in reaction (~~2~~33~~6~~).

$$2C_{12}A_7 = 5C_3A + 9CA \qquad (\cancel{2}33\cancel{6})$$

As reported in literature [34], the Gibbs energy changes for reaction (~~2~~33~~6~~) is -1.5, -2.0, and -3.5 kJ/mole CaO at 1700 K (1427 °C), 1600 K (1327 °C), and 1500 K (1227 °C), respectively. Therefore, C_3A and CA phases formation upon cooling was favorable.

2. In the present work, as indicated by the strongest intensity in XRD in Fig. 4, the primary crystallized phase from G-Slag is $C_{12}A_7$. As it has significant amount, it may absorb the required oxygen during precipitation and eventually become more stable. From this reason, we may say that unless the composition of the binary slag is on the range of its primary crystallization (about 46 - 51 wt pct Al_2O_3) or as the majority phase in the system, the $C_{12}A_7$ phase is likely unstable even in oxidizing atmosphere.

According to the XRD results in Fig. 4, no CAS_2 phase in I-Slag is observed, which does not agree with the ternary system at 101.3 kPa (1 bar) in Fig. ~~17~~18. CAS that is observed is known as Calcium Tschermak's pyroxene (CATs) for geologists, which is one of the important constituent of the earth's upper mantle and of the natural aluminous pyroxenes. The crystallography pattern of CAS in present work matched against the measurement of Okamura et al [38] that is a = 9.609 Å, b = 8.652 Å, c = 5.274 Å, β = 106.06 °, V = 421.35 $Å^3$, in monoclinic *C2/c* space group. The CAS phase is formed by a solid-state reaction as seen in reaction (34~~27~~) and (35~~28~~). Okamura et al. [38] synthesized a single crystal of CAS from CAS_2, C_2AS, and Al_2O_3 after heating the mixture at 1573 K (1300 ^{o}C) within 24 hours in 18.10^5 kPa (18 kbar). On the other hand, Hariya and Kennedy [39] observed that CAS_2 decomposes to CAS and SiO_2 under high pressure and temperature.

$$CAS_2 + C_2AS + Al_2O_3 = 3CAS \qquad (34\cancel{27})$$

$$CAS_2 = CAS + SiO_2 \qquad (35\cancel{28})$$

Many works concluded that CAS is a high-pressure and temperature phase [38] [40]. In addition, Hays [41] reported that pure CAS is not stable below 1433 K (1160 ^{o}C) and the pressure field of stability is relatively narrow even at higher temperature. However, Ma et al. [42] stated that although synthetic CAS is a high-pressure phase, a natural CAS could be found in low-pressure atmosphere. Fig. 9 (c) shows that I-Slag does not have lamellar structure, which indicates the phases were not formed through a slow diffusion mechanism. Thus, in contrary to the conclusion that was given by some researchers above, we suggest that the reaction (34~~28~~) may occur during the cooling of a congruently melted CAS_2 phase on ambient pressure. The co-existing phases of CAS and SiO_2 in XRD result of I-Slag worth as the evidence of the argument. Nevertheless, this hypothesis needs further investigation.

IV.7. Phase changes upon slag solidification and cooling

In Table 7, the WDS analysis of B-Slag on dark and bright structure is identical with the phase of C_2AS and $CaTiO_3$, respectively. The WDS result on fine lamellar phase indicates a C_2AS phase as it has similar composition with the dark phase, only it has more TiO_2. This may not be precise, as the lamellar is constructed with dark and less-bright phase. It is difficult to identify the composition of each layer as the thickness is as much as 2 µm. To understand the existing phases in lamellar structure, a crystallization path of B-Slag becomes necessary. Based on alkemade line and phase lever-rule we can describe it as follows:

1. Consider we have 100 g of slag with the composition of 50 wt pctAl_2O_3, 12 wt pctSiO_2, and 38 wt pctCaO, which is a normalized XRF data of B-Slag from Table 5. At 1923 K (1650 °C), slag liquid phase exists, named liquid #1.

2. From 1923 K (1650 °C) to 1783 K (1510 °C) the primary crystallization of C_2AS occurs; liquid #1 → C_2AS + liquid #2. The slag consists 14 g of C_2AS phase (14 pct) and 86 g of liquid #2 phase (86 pct).

3. From 1783 K (1510 °C) to 1623 K (1350 °C), following reaction occurs: liquid #2 → C_2AS + CA + liquid (p). At this stage lamellar structure co-exists. The mass of C_2AS, CA, and liquid (p) phase is 30.1 (35 pct), 49 (57 pct), and 6.9 g (8 pct), respectively.

4. At 1623 K (1350 °C), liquid (p) + $C_2AS \rightarrow C_2S$ + CA, a peritectic reaction occurs. At current stage the remaining liquid is consumed, as well as the partial of C_2AS phase. The mass of liquid (p), C_2AS, C_2S, and CA phase is 6.9 g (66 pct), 3.55 (34 pct), 3.86 (37 pct), and 6.59 g (63 pct), respectively.

5. From 1623 K (1350 °C) to room temperature, at the solidus line no liquid exist and impurities may segregate and concentrated between the primary C_2AS grains. Total amount of condensed phases in B-Slag is:

C_2AS = 14 g + 30.1 g - 3.55 g = 40.55 g (40.6 pct)
CA = 49 g + 6.59 g = 55.59 g (55.6 pct)
C_2S = 3.86 g (3.8 pct)
Total = 100 g (100 pct)

On the other hand, coarse and small grain structure in G-Slag indicates the $C_{12}A_7$ phase. Grzymek et al. ~~[43]~~[43] observed that $C_{12}A_7$ has polymorphic transition phase depends on the synthesizing temperature, condition of atmosphere (reducing or oxidizing), and the cooling rate when it was formed. Grzymek mentioned that when synthesize held in an oxidizing atmosphere at 1770 K (1497 ^{o}C), and then slowly cooled, the structure is isotropic and grainy-ish with an anisotropic phase formed on grain boundaries, which is similar to present result. The structure of CA phase in G-Slag is indistinguishable as the amount is considerably low.

In I-Slag, pointed WDS analysis on bright and dark structures correspond to CAS phase with insignificant difference on TiO_2 amount (1-2 wt pct). No lamellar structure is shown as it was in B-Slag. An X-ray element mapping on I-Slag in Fig. ~~8~~7 shows the dark structure has high concentration in titanium and it has stronger bond to aluminum than of calcium and silicon. Interestingly, these complex oxides do not behave similarly in G-Slag. The area of the phase that is rich in titanium have tendency to bond with calcium and silicon than aluminum, as seen in Fig. 6, which is supported by SEM and EDS results for G-Slag in Fig. 8. This gives valuable information for the leachability of the slag, as the titanium that bonded to the aluminum might hinder the alumina-leaching efficacy.

As we observed above the slags B, G, and I contain different Al_2O_3-containing phases and the leachability of them is important for alumina extraction. The leaching behavior of $C_{12}A_7$ and CA phase have been studied in literature and the main point to be mentioned here is both phases are soluble in sodium carbonate solution and therefore is favorable for the alumina recovery. Lundquist and Leitch [45] proposed the leaching reaction of CA phase where~~As we observed above the slags B-, G-, and I contain different Al_2O_3-containing phases and the leachability of them is important for alumna extraction. The leaching behavior of …,…,…have been studied in literateure and the main points to be mention are~~

$$CaO\cdot Al_2O_3 + Na_2CO_3 + 4H_2O = CaCO_3 + 2Na^+ + 2Al(OH)^{4-} \quad (36)$$

~~…,…,…~~

While for $C_{12}A_7$ phase the reaction may be described as follows [8]:

$$12CaO\cdot 7Al_2O_3 + 12Na_2CO_3 + 5H_2O = 7Na_2O\cdot Al_2O_3 + 12CaCO_3 + 10NaOH \quad (37)$$

However, ~~there is no literature~~ no publication was found about the leachability of ~~…,…,…~~CAS, C_2AS, and C_5A_3 phases. This will be the subject of study of the authors in near future. Understanding the leaching behavior of Al_2O_3-containing phases may pave the way to treat different metallurgical slags, which is quite important regarding the sustainable process development and circular economy.

~~As we observed above the slags B-, G-, and I contain different Al2O3-containing phases and the leachability of them is important for alumna extraction. The leaching behavior of …,…,…have been studied in literateure and the main points to be mention are…,…,… However, there is no literature about the leachability of …,…,…phases. This will be the subject of study of the authors in near future. Understanding the leaching behavior of Al2O3-containing phases may pave the way to treat different metallurgical slags, which is quite important regarding the sustainable process development and circular economy.~~

Formatted: Justified

Formatted

Formatted

Formatted

Formatted

Formatted

Formatted

V. Conclusion

The characteristics of calcium aluminate-containing slags and pig iron produced from low grade bauxite ores were studied. Using advance characterization techniques, the thermochemistry of oxides reduction, elements distribution between the slag and metal products, and mechanisms of the formation of phases in them can be explained. The main conclusions can be summarized as follows:

1. Iron from the ores is removed from 94.8 to 99.9 pct during smelting-reduction by carbon and yields the alumina-containing slag containing less than 1 wt pctFe, dependent on the slag chemistry.

2. The partial separation of Mn, Si, Ti, V and P oxides occurs through the smelting-reduction, where low distribution coefficients of L_{Mn}, L_{P}, and L_{V} are observed, While L_{Si} and L_{Ti} values ranges are considerably wide depend on the characteristics of the produced slag.

3. The viscosity in calcium-aluminate slags with CaO/SiO_2 mass ratio less than three is higher compared to other compositions at elevated temperatures. It causes less of Fe-removal and gives more porous product.

4. Silicon loss from high SiO_2-containing bauxites may occur at elevated temperatures through the SiO gas formation.

5. The leachable slag phases ($CaO\cdot Al_2O_3$, $12CaO\cdot 7Al_2O_3$), which are observed in G-Slag, are obtained after the smelting-reduction of bauxite that has $Al_2O_3/(Fe_2O_3 + SiO_2)$ mass ratio higher than two with up to 5 $K\cdot s^{-1}$ of cooling rate.

6. The complex bonding between titanium and aluminum oxides in slag is not favorable for leaching process and is likely to occur in $CaO\cdot Al_2O_3\cdot SiO_2$ phase.

Acknowledgement

Authors acknowledge Hanne Sellæg for her valuable contribution in the laboratory works. The present research has been funded by NTNU and co-sponsored by Research Domain 5–Materials and Society in SFI Metal Production (a Norwegian Centre for Research-driven Innovation in metal production) through project number 237738.

References

[1] K. Tsesmelis: *Proceedings of 35th International ICSOBA Conference*, 2017, vol. 42, pp. 71.

[2] D. J. Roth and J. Falter: *Proceedings of 35th International ICSOBA Conference*, 2017, vol. 42, pp. 539-45.

[3] E. Ujaczki, P. Cusack, S. Clifford, T. Curtin, R. Courtney and L. O'Donoghue: *Proceedings of 35th International ICSOBA Conference*, 2017, vol. 42, pp. 485-90.

[4] B. Bhoi, P. Rajput and C. R. Mishra: *Proceedings of 35th International ICSOBA Conference*, 2017, vol. 42, pp. 565-74.

[5] T. Hertel, B. Blanpain and Y. Pontikes: *Proceedings of 35th International ICSOBA Conference*, 2017, vol. 42, pp.575-85.

[6] H. Pedersen: *United States of America Patent*, 1927, 1618105.

[7] J. Safarian and L. Kolbeinsen: *Sustainable Industrial Processing Summit*, 2016, pp. 149-158.

[8] H. E. Blake Jr., O. C. Fursman and A. D. Fugate: *US Bureau of Mines*, 1966, pp. 1-19.

[9] T. Hignett: *Industrial and Engineering Chemistry*, 1947, vol. 39, pp. 1052-60.

[10] J. Miller and A. Irgens: *Light Metals*, 1974, pp. 977-82.

[11] R. Lundquist and H. Leitch: *US Bureau of Mines*, 1964, pp. 1-16.

[12] F. I. Azof, L. Kolbeinsen and J. Safarian: *Proceedings of 35th International ICSOBA Conference*, 2017, vol. 42, pp. 243-53.

[13] K. Kyriakogona, I. Giannopoulou and D. Panias: *Proceedings of the 3rd World Congress on Mechanical, Chemical, and Material Engineering*, 2017, pp. 1331-6.

[14] H. Sellæg, L. Kolbeinsen and J. Safarian: *Light Metals*, 2017, pp. 127-135.

[15] S. H. Ahn, Y. H. Kim, J. P. Shin and Y. E. Lee: *ISIJ International*, 2014, vol. 54, pp. 750-55.

[16] B. Hallstedt: *Journal of the American Ceramic Society*, 1990, pp. 15-23.

[17] K.-S. Chou: *Retrospective theses and dissertations, Digital Repository of Iowa State University*, 1979, pp. 1-152.

[18] A. Pehlivan, A. O. Aydin and A. Alp: *Sakarya University Journal of Science*, 2012, pp. 92-8.

[19] A. W. A. Al-Ajeel and S. I. Al-Sindy: *Iraqi Bulletin of Geology and Mining*, 2006, vol. 2, pp. 67-76.

[20] J. Xiao, F. Li, Q. Zhong, H. Bao, B. Wang, J. Huang and Y. Zhang: *Hydrometallurgy*, 2015, pp. 118-124.

[21] P. Smith: *Hydrometallurgy*, 2009, pp. 162-176.

[22] M. Jiayu, L. Zhibao and X. Qinggui: *American Institute of Chemical Engineers*, 2012, vol. 58, pp. 2180-91.

[23] H. E. Blake Jr., O. C. Fursman, A. D. Fugate and L. H. Banning: *US Bureau of Mines*, 1968, pp. 1-19.

[24] Z. Tong, Y. Li and L. Lian: *Light Metals*, 2012, pp. 185-88.

[25] B. Wang, H.-l. Sun, D. Guo and S.-w. Bi: *Light Metals*, 2011, pp. 201-4.

[26] R. Pomfret and P. Grieveson: *Canadian Metallurgical Quarterly*, vol. 22, pp. 287-299, 1983.

[27] S. Teasdale and P. Hayes: *ISIJ International*, 2005, vol. 45, pp. 634-41.

[28] J. Safarian, L. Kolbeinsen, M. Tangstad and G. Tranell: *Metallurgical and Materials Transactions B*, 2009, vol. 40B, pp. 929-39.

[29] M. Sumito, N. Tsuchiya and K. Okabe: *Transactions ISIJ*, 1981, vol. 21, pp. 414-21.

[30] M. Kowalski, P. Spencer and D. Neuschutz: *Slag atlas 2nd edition*, Dusseldorf: Verlag Stahleisen GmbH, 1995.

[31] H.-l. Sun, B. Wang, H.-y. Yu, S.-w. Bi and G.-f. Tu: *Light Metals*, 2010, pp. 29-32.

[32] B. Wang, H.-l. Sun, X.-z. Zhang and S.-w. Bi: *Light Metals*, 2011, pp. 241-44.

[33] G. Rankin and F. Wright: *American Journal Science*, 1915, vol. 39, pp. 1-79.

[34] R. Nurse, J. Welch and A. Majumdar: *Transaction of British Ceramics Society*, 1965, pp. 323-32.

[35] E. Haccuria, T. Crivits, P. C. Hayes and E. Jak: *American Ceramic Society*, 2015, vol. 99, pp. 691-704.

[36] J. Imlach, L. Glasser and F. Glasser, *Cement and Concrete Research*, 1971, vol. 1, pp. 57-61.

[37] H.-l. Sun, B. Wang, J.-x. Zhang and S.-f. Zong: *Advances in Materials Science and Engineering*, 2014, pp. 1-6.

[38] F. P. Okamura, S. Ghose and H. Ohashi: *American Mineralogist*, 1974, vol. 59, pp. 549-57.

[39] Y. Hariya and G. Kennedy: *American Journal of Science*, 1968, vol. 266, pp. 193-203.

[40] B. J. Wood: *American Mineralogist*, 1976, vol. 61, pp. 599-602.

[41] J. F. Hays: *Carnegie Institution Washington Year Book*, 1965, pp. 234-239.

[42] C. Ma, S. B. Simon, G. R. Rossman and L. Grossman: *American Mineralogist*, 2009, vol. 94, pp. 1483-92.

[43] J. Grzymek, A. Grzymek, Z. Konik, A. Stok and M. Gawlicki: *Light Metals*, 1985, pp. 87-99.

[44] H. Mao, M. Hillert, M. Selleby and B. Sundman: *Journal of the American Ceramic Society*, 2006, vol. 89, pp. 298-308.

[45] R. V. Lundquist and H. Leitch: *US Bureau of Mines*, 1963, pp. 1-9.

Formatted: English (U.S.)

Formatted: Font: Italic

Formatted: English (U.S.)

List of Tables

List of Figures

Fig. 1. An overview of Pedersen process.

Fig. 2. XRD analysis of B-, G-, and I-Bauxites.

Fig. 3. Cross section view of the solidified slag and pig iron produced from B-, G-, and I-Bauxite.

Fig. 4. XRD analysis on B-, G-, and I-Slag.

Fig. 5. X-ray element mapping of B-Slag.

Fig. 6. X-ray element mapping of G-Slag.

Fig. 7. X-ray element mapping of I-Slag.

Fig.8. BSE image of G-Slag with the corresponding EDS quantified analysis at (a), (b), and (c) area.

Fig.8(a). EDS analysis of the dark-bright area (a) in Fig.8.

Fig.8(b). EDS analysis of point (b) in Fig.8.

Fig.8(c). EDS analysis of point (c) in Fig.8.

Fig. 9. BSE images of: (a) B-Slag, (b) G-Slag, and (c) I-Slag.

Fig. 10. BSE image of cross-section of B-Slag and adjacent B-Pig iron.

Fig. 11. BSE images showing the main co-existing phases in (a) B-; (b) G-; and (c) I-Pig iron samples.

Fig. 12. Illustration of FeO and SiO_2 reduction by carbothermic reaction at slag/gas, gas/metal and slag/metal interface.

Fig. 13. The calculated phases in equilibria at different temperatures for: (a) B-Bauxite; (b) G-Bauxite; and (c) I-Bauxite setups.

Fig. 14. Correlation between basicity (C/S) and viscosity in different C-A-S slags at different temperatures.

Fig. 15. Distribution of phases in bauxite ores and slags after smelting-reduction.

Fig. 16. The changes of δG_{11} and δG_{26} at 1873 K in different mol pct Ti.

Fig. ~~16~~17. Distribution coefficient of several elements in different bauxites.

Fig. ~~17~~18. Isothermal projection of ternary $CaO-Al_2O_3-SiO_2$ system.

Fig. ~~18~~19. Part of $CaO-Al_2O_3$ binary system where (a) the $C_{12}A_7$ phase is included, and (b) a moisture-free without formation of $C_{12}A_7$ phase, as simulated by FactSage™.

Formatted: Space After: 0 pt, Line spacing: Double

Formatted: Left

Formatted: Font: Check spelling and grammar

Formatted: Normal, Tab stops: Not at 6.26"

Table 1. Characteristics of lime and coke as received.

Composition	**Lime (wt pct)**	**Coke (wt pct)**
Al_2O_3	0.3	2.8
Fe	NA	0.6
Fe_2O_3	NA	0.9
SiO_2	1.0	5.6
TiO_2	NA	0.1
CaO	54.0	0.4
MgO	1.0	0.2
Mn	NA	0.03
MnO	NA	0.04
K_2O	0.1	0.2
C-Fix	NA	87.7
CO_2 (as carbonate)	47.5	NA
P	10 ppm	0.1
S	110 ppm	0.4
H_2O	1.0	15.5
Volatile matter	NA	1.53
Trace elements	100 - sum	100 - sum

Table 2. XRF analysis of different bauxite ores.

Element	**Bauxite Ore**		
	B (wt pct)	**G (wt pct)**	**I (wt pct)**
Al	18.4	31.0	14.7
Fe	8.3	14.2	14.3
Si	22.2	3.4	23.9
Ti	3.3	3.4	4.3
Mg	0.1	0.3	0.2
Ca	NA	5.6	0.1
K	130 ppm	433 ppm	0.1
Mn	0.1	323 ppm	273 ppm
P	0.0	91 ppm	346 ppm
O*	100 - sum	100 - sum	100 - sum
LOI	~16.1	~14.6	~10.9

**oxygen presents as oxides*

Table 3. Normalized XRF analysis of the calcined bauxites to the corresponding stable oxides.

Phase	**Calcined Bauxite**		
	B (wt pct)	**G (wt pct)**	**I (wt pct)**
Al_2O_3	44.2	65.4	35.7
Fe_2O_3	15.2	22.7	26.2
SiO_2	36.2	4.1	32.8
TiO_2	4.2	3.2	4.6
MgO	0.1	0.2	0.2
CaO	NA	4.4	0.1
K_2O	NA	NA	0.2
MnO	0.1	NA	NA

Table 4. Mass changes of B-, G- and I-Bauxite setup after smelting trial.

Condition	**B-Bauxite (kg)**	**G-Bauxite (kg)**	**I-Bauxite (kg)**
Crucible and materials, before smelting^(a)	8.76	9.26	7.74
Crucible and materials, after smelting^(b)	7.34	7.84	7.27
Total mass loss: *(a) - (b)*	1.42 (16.3 pct)	1.42 (15.4 pct)	0.47 (6.1 pct)
Materials before smelting^(c)	2.80	3.26	1.71
Materials after smelting^(d)*:* *(b) - graphite crucible mass loss**	1.64	1.98	1.24
Measured materials mass loss: *(c) - (d)*	1.16 (41.5 pct)	1.28 (39.4 pct)	0.47 (21.2 pct)

**The mass loss pct of the graphite crucible and graphite rod after one hour of smelting trial are 2.2 ± 0.5 pct and 4 pct, respectively.*

Table 5. Normalized XRF analysis of the obtained slags in smelting-reduction.

Phase	**Slag**		
	B (wt pct)	**G (wt pct)**	**I (wt pct)**
Al_2O_3	47.5	46.1	36.7
SiO_2	11.2	2.3	30.3
TiO_2	0.9	1.8	2.8
MgO	0.4	0.5	0.5
CaO	36.8	48.1	28.0
K_2O	NA	NA	0.5
MnO	NA	NA	0.1
FeO	0.01	0.44	1.4
Trace elements	NA	NA	NA

Table 6. XRF analysis of pig iron samples resulted from smelting-reduction treatment.

Element	Pig Iron		
	B (wt pct)	**G (wt pct)**	**I (wt pct)**
Fe	89.9	92.0	92.7
C_{sat}	4.6	5.3	4.9
Si	4.0	0.2	1.2
Mn	0.5	0.2	0.4
Ti	0.6	0.9	0.2
V	0.1	0.2	0.1
Cr	0.1	0.5	0.1
P	450 ppm	950 ppm	0.1
S	NA	70 ppm	70 ppm
Trace elements	100 - sum	100 - sum	100 - sum

Table 7. WDS analysis of phases observed in B-, G-, and I-Slags structures shown in Fig.~~10~~9.

Point no.	**CaO (wt pct)**	**Al_2O_3 (wt pct)**	**SiO_2 (wt pct)**	**TiO_2 (wt pct)**	**MgO (wt pct)**	**FeO (wt pct)**	**V_2O_3 (wt pct)**	**MnO (wt pct)**	**P_2O_5 (wt pct)**	**K_2O (wt pct)**
(a)1-3	42.66	35.05	21.62	0.33	0.29	NA	NA	0.01	0.03	NA
(a)4-6	42.99	34.72	21.41	0.61	0.23	0.01	0.01	0.01	0.01	0.01
(a)7-9	55.29	6.00	4.20	31.12	2.93	NA	0.26	0.19	NA	0.01
(b)1-3	49.58	48.99	0.79	0.32	0.24	0.01	0.01	0.03	0.03	NA
(b)4-6	48.94	42.66	2.73	4.35	1.12	0.04	0.05	0.07	0.04	NA
(c)1-3	30.81	32.35	33.95	1.36	0.41	0.10	0.03	0.12	0.02	0.85
(c)4-6	28.43	33.86	33.50	2.87	0.67	0.04	0.03	0.10	0.01	0.49

Table 8. WDS analysis of phases in B-Pig iron shown in Fig. ~~11~~10.

Point no.	**Fe (wt pct)**	**C (wt pct)**	**Mn (wt pct)**	**Si (wt pct)**	**Ti (wt pct)**	**Mg (wt pct)**	**V (wt pct)**	**Al (wt pct)**	**P (wt pct)**	**Others (wt pct)**
1	90.5	4.9	1.1	2.9	NA	0.1	0.3	NA	0.2	NA
2	90.5	4.6	1.1	3.1	0.1	0.1	0.3	NA	0.2	NA
3	2.8	13.1	NA	0.5	80.4	0.0	2.9	0.1	NA	0.2
4	2.3	15.0	NA	0.1	79.4	0.1	2.3	0.2	NA	0.6

Table 9. Correlation between starting materials mass loss with their causes.

Materials Mass Loss Causes	**B-Bauxite setup (kg)**	**G-Bauxite setup (kg)**	**I-Bauxite setup (kg)**
Total materials mass loss as measured$^{(1)}$	1.16	1.28	0.47
LOI of Bauxite^{a}	0.28	0.25	0.12
LOI of Lime^{b}	0.45	0.66	0.23
LOI of Coke^{c}	2.10^{-3}	2.10^{-3}	2.10^{-3}
Total loss due to LOI$^{(2)}$: $a + b + c$	0.74	0.92	0.36
Mass loss due to reduction$^{(3)}$	0.16	0.21	0.16
Theoretical mass loss/measured mass loss: *(3)/(1)*	0.77	0.87	1.10